

**POLITECNICO DI MILANO**

Faculty of Industrial and Information Engineering

Laurea Magistrale (MSc) in Engineering Physics



**Development of a three-arm integrated  
photonic interferometer for quantum sensing  
applications**

*Supervisor:* **Dr. Roberto Osellame**

*Co-supervisor:* **Dr. Giacomo Corrielli**

*Thesis of:*

**Martina Riva**

**Student ID: 837181**

*Academic Year 2016/17*



# Abstract

Quantum metrology is an emerging area of metrology, the science of measurements, in both theoretical and experimental aspects. It is focused mainly in the development of new methods of measurements, especially employing quantum techniques. In this way it is possible to achieve an enhancement in the measured parameter estimation, overcoming the bounds that classical physics imposes.

The aim of this thesis work is the design, the fabrication and the characterization of an integrated three modes Mach-Zehnder interferometer, with actively reconfigurable phases. Such a device is the ideal platform for testing several quantum metrology algorithms for simultaneous multi-parameters estimation, if probed with non-classical states of light. The fabrication technique adopted is that of Femtosecond Laser Micromachining (FLM): a cost effective and very reliable fabrication method for producing high quality optical circuits with complex geometries, ideal for scientific investigation purposes. Besides the design and the fabrication details, we also present here a full characterization of the three-arms interferometer with classical light, which validates its correct functioning.



# Introduzione

La metrologia è la scienza della misurazione, dalla definizione delle unità di misura alla realizzazione dei loro campioni, fino allo sviluppo di nuovi metodi di misurazione.

Specialmente durante gli ultimi decenni è stata sviluppata un'area denominata metrologia quantistica la quale sfrutta le leggi della meccanica quantistica in modo da migliorare l'accuratezza nella misura di un certa grandezza. In particolare lo scopo è quello di superare il limite standard (Standard Quantum Limit, SQL) che pone il limite classico alla precisione con la quale una misura può essere effettuata. Tale limitazione è dovuta essenzialmente alla presenza di rumore, specialmente a quello shot.

Le applicazioni pratiche in questo ambito sono in crescita. Quella di maggior successo fin'ora riguarda il rilevamento delle onde gravitazionali grazie a un apparato interferometrico ben studiato e l'utilizzo di stati quantistici squeezed. Altre applicazioni si possono trovare in biologia, specialmente riguardo l'imaging, la sincronizzazione di orologi, la litografia, etc.

Il lavoro presentato in questa tesi riguarda la progettazione, la fabbricazione e la caratterizzazione di un dispositivo fotonico integrato di un dispositivo integrato per la fotonica che ha lo scopo di misurare simultaneamente due parametri, con un miglioramento nella loro stima grazie all'impiego di tecniche quantistiche. Il dispositivo in oggetto è un interferometro a tre braccia scritto in un substrato di vetro attraverso la tecnica di Femtosecond Laser Micromachining (FLM), tecnica che permette di ottenere grande flessibilità e stabilità del circuito prodotto.

La tesi è composta da diversi capitoli. I primi tre sono focalizzati sui concetti di base e sulle conoscenze teoriche utili alla comprensione dell'esperimento

realizzato. In particolare nel Capitolo 1 sono discusse le basi della metrologia quantistica e alcune sue applicazioni, mentre nel Capitolo 2 e 3 sono presentati in maggior dettaglio la tecnica di FLM e i setup e metodi di fabbricazione e caratterizzazione impiegati. Nei capitoli successivi, invece, è discussa in modo approfondito la fabbricazione dell'interferometro a tre braccia. In particolare nel Capitolo 4 è spiegato lo scopo dell'esperimento e il progetto generale del circuito che vuole essere sviluppato. Nel Capitolo 5 è trattata la fabbricazione del tritter, l'elemento base che compone l'interferometro a tre braccia. La realizzazione finale e caratterizzazione del dispositivo completo sono presentati nel Capitolo 6.

L'esperimento finale, che prevede l'utilizzo del dispositivo fabbricato con stati di luce non classica, sarà condotto presso i laboratori di ottica quantistica del Dipartimento di Fisica dell'università La Sapienza di Roma, ed esula dagli scopi di questo lavoro di tesi.

# Contents

<b>Contents</b>	<b>v</b>
<b>List of Figures</b>	<b>ix</b>
<b>List of Tables</b>	<b>xi</b>
<b>Introduction</b>	<b>1</b>
<b>1 Quantum Mechanics and Metrology</b>	<b>3</b>
1.1 Quantum Metrology . . . . .	5
1.1.1 Optical measurements and Standard Quantum Limit . . . . .	5
1.1.2 Fundamental Quantum Limit . . . . .	6
1.1.3 Phase sensitivity, resolution and Fisher information . . . . .	8
1.1.4 Limitations . . . . .	9
1.2 Phase detection . . . . .	10
1.2.1 Beam splitter: classical and quantum view . . . . .	10
1.2.2 MZI: classical approach . . . . .	11
1.2.3 MZI: single photon interference . . . . .	13
1.2.4 Improvement with NOON state (N=2) . . . . .	14
1.2.5 General improvement employing NOON state . . . . .	16
1.2.6 Multiparameter estimation . . . . .	17
1.3 Applications . . . . .	17
1.3.1 Quantum biology . . . . .	17
1.3.2 Quantum imaging . . . . .	18
1.3.3 Quantum frequency . . . . .	19

1.3.4	Quantum positioning and clock synchronization . . . . .	20
1.3.5	Gravitational waves detection . . . . .	21
<b>2</b>	<b>Femtosecond Laser Micromachining</b>	<b>23</b>
2.1	Introduction . . . . .	24
2.1.1	Femtosecond laser interaction . . . . .	24
2.2	Fabrication parameters . . . . .	26
2.2.1	Pulse energy and translation speed . . . . .	26
2.2.2	Repetition rate . . . . .	27
2.2.3	Focusing conditions . . . . .	28
2.3	Photonic devices . . . . .	29
2.3.1	Directional couplers . . . . .	30
2.3.2	Tritter . . . . .	32
2.3.3	Mach Zehnder and multi-port interferometers . . . . .	33
2.3.4	Thermo-optic phase shifter . . . . .	34
<b>3</b>	<b>Experimental Setup</b>	<b>37</b>
3.1	Fabrication Setup . . . . .	38
3.1.1	Laser source . . . . .	38
3.1.2	Translation stage . . . . .	40
3.2	Characterization Setup . . . . .	40
3.2.1	Optical microscope . . . . .	40
3.2.2	Device coupling . . . . .	41
3.2.3	Mode profile . . . . .	42
3.2.4	Losses measurement . . . . .	43
<b>4</b>	<b>On Chip Quantum Estimation of Two Phases</b>	<b>47</b>
4.1	Goal of the Experiment . . . . .	48
4.1.1	Mathematical description . . . . .	48
4.1.2	Phase estimation . . . . .	50
4.2	Design of the chip . . . . .	51
<b>5</b>	<b>Tritter</b>	<b>53</b>
5.1	Optimization of the fabrication parameters . . . . .	54



5.1.1	Choice for the fabrication parameters . . . . .	54
5.1.2	Bending losses . . . . .	55
5.2	Tritter parameters . . . . .	56
5.2.1	Coupling lengths . . . . .	56
5.2.2	Phase . . . . .	56
<b>6</b>	<b>Three-arm interferometer</b>	<b>63</b>
6.1	Interferometer design . . . . .	64
6.1.1	Thermo-optic phase shifters . . . . .	65
6.2	Connectorization method . . . . .	68
6.3	Characterization method . . . . .	70
6.4	Experimental data . . . . .	72
6.4.1	Data acquisition . . . . .	73
6.4.2	Determination of the $\alpha$ coefficients . . . . .	75
6.4.3	Interferometer's map . . . . .	77
	<b>Conclusion</b>	<b>81</b>



# List of Figures

1.1	Classical and Quantum measurement's strategies . . . . .	8
1.2	Mach-Zehnder interferometer . . . . .	12
1.3	Ghost image . . . . .	19
1.4	Gravitational waves noise . . . . .	22
2.1	Non-linear light absorption processes . . . . .	25
2.2	Directional couplers . . . . .	30
2.3	Tritters . . . . .	33
2.4	Interferometers . . . . .	35
3.1	Fabrication setup . . . . .	39
3.2	Device coupling . . . . .	41
3.3	Acquisition spatial intensity . . . . .	42
4.1	Decoupled tritter . . . . .	49
4.2	Basic design three-arm interferometer . . . . .	50
4.3	Three-arm interferometer . . . . .	51
5.1	Bending losses . . . . .	55
5.2	Directional couplers . . . . .	57
5.3	Tritter geometry . . . . .	58
5.4	Comparison: experiment and theory . . . . .	59
5.5	Active tritter . . . . .	61
5.6	Outputs dynamic tritter . . . . .	62
5.7	Tritter picture . . . . .	62

6.1	Non-linear light absorption processes . . . . .	65
6.2	Interferometer's design . . . . .	66
6.3	Simulation: $\alpha$ matrix . . . . .	67
6.4	Resistors . . . . .	69
6.5	Connectorization method . . . . .	70
6.6	Parameters setting . . . . .	71
6.7	Setup . . . . .	73
6.8	Input/Output setting . . . . .	74
6.9	Theoretical data . . . . .	74
6.10	Experimental data . . . . .	75
6.11	Interferometer's fringes . . . . .	76
6.12	Fourier transform . . . . .	77
6.13	Interferometer's map . . . . .	78
6.14	Interferometer's map 2 . . . . .	79
6.15	Interferometer's map 3 . . . . .	79

# List of Tables

5.1	Parameters for waveguides at 780 nm . . . . .	55
5.2	Passive phase and relative angle . . . . .	60



# Introduction

Metrology is the science of measurement and it regards several aspects, from the standardization of the unity of measurements, their definition and realization of standards till the development of new methods of measurement.

It is especially during the last decades that has been developed a research area named quantum metrology. Quantum metrology exploits the law of quantum mechanics in order to improve the accuracy of the measurement of a certain quantity. In particular its aim is to go beyond the Standard Quantum Limit (SQL) which is the bound for classical measurements due to the presence of noise, especially the shot noise.

The practical applications in this field are growing up. The one of most success until now is the detection of gravitational waves thanks to a well-studied interferometric apparatus and the employing of quantum squeezed states. Other applications can be found in biology, especially regarding the imaging, clock synchronization, lithography, etc.

The work presented in this thesis concerns the design, fabrication and characterization of an integrated photonic device in order to measure two parameters simultaneously with an enhancement in their estimation thanks to the employment of quantum techniques. The device is a three-arm interferometer written in a glass substrate through the Femtosecond Laser Micromachining (FLM) technique, which lets to achieve great flexibility and stability of the circuit.

The thesis is divided in several chapters. The firsts three are focused on the basics and theoretical background. In particular in Chapter 1 are discussed the basics of quantum metrology and some of its applications, while in Chapter 2 and 3 are presented in more details the FLM technique, the

fabrication and characterization setups employed in the development of the integrated circuits. In the following chapters, instead, is discussed in detail the fabrication of the three-arm interferometer. In Chapter 4 it is explained the aim of the experiment and the general design of the circuit. In Chapter 5 there is a full treatment regarding the fabrication of a tritter, the basic element that composed the three-arm interferometer. The final realization and characterization of the complete device is presented in Chapter 6.

The final experiment, which will employ no-classical light states, will be conducted in the quantum optics laboratories of the Physics Department of La Sapienza University of Rome, but lies outside the aim of this thesis work.



# Chapter 1

## Quantum Mechanics and Metrology

Metrology is “*the science of measurement, embracing both experimental and theoretical determinations at any level of uncertainty in any field of science and technology*”, by the definition of the International Bureau of Weights and Measures [1] (BIPM). This organization has the duty to maintain the International System of Units (SI) under the terms established in the 1875 by the Metre Convention. It is thanks to this international treaty that we had the birth of the metric system, which has been shared by many countries.

The situation in more ancient times was quite chaotic, since every country had its own measurement system or subjective units of measure. For instance the evaluation of distances by feet or hands, without a proper standard, to be compared to could bring to many misunderstandings. In order to overcome this problem, many ancient empires already developed a local standardization but it was valid just under their domains so that the external communications were quite difficult.

Modern metrology, as mentioned above, put its root during the French Revolution and has lead, finally, to a conformity in the international units of measurement.

The progresses in science and technology have brought to a continuous improvement of metrology, like a more accurate definition of the measurement

standards. Nowadays for example the second is defined as “the duration of 9192631770 periods of the radiation corresponding to the transition between two specific hyperfine levels of the ground state of the cesium 133 atom” and not anymore as fraction of the day, year or by a mechanical clock.

Metrology does not concern just about the establishment of units of measurement and the realization of standards, but also the traceability of these lasts, and the development of new measurement methods. In particular, traceability is the “*property of a measurement result whereby the result can be related to a reference through a documented unbroken chain of calibrations, each contributing to the measurement uncertainty*” as state by the Joint Committee for Guides in Metrology [1]. Thus, through this unbroken chain of comparisons, it is possible to refer any measurement to its original definition even though with a certain uncertainty.

This concept of uncertainty is highly correlated with the method of measurement adopted and, in particular during the last years, quantum metrology has pushed this limit towards the minimum achievable, as we will show in the next sections.

## 1.1 Quantum Metrology

Quantum metrology aims to improve the precision on the measurement exploiting quantum strategies and, in this way, overcome the Standard Quantum Limit [2]. We start now to present how a measurement is performed and which are its limitations. Then we will focus on the measurements performed by means of light, highlighting how it could be used for quantum metrology purposes.

### 1.1.1 Optical measurements and Standard Quantum Limit

Usually, a measurement process is made repeating it  $N$  times and averaging the results, so that the statistical error on the estimation of the measured parameter can be reduced. This reduction is anyway limited, as declared by the central limit theorem<sup>1</sup>, to:

$$\Delta\varphi > \frac{1}{\sqrt{N}} \quad (1.1)$$

which is the so-called Standard Quantum Limit (SQL), and where  $\Delta\varphi$  is the statistical error of the parameter  $\varphi$ . It is important to notice that the central limit theorem holds for independent and identically distributed random variables, so it describes the case of Poisson processes. We will now focus on optical measurements and the sources of noise that have more to deal with them, such as the shot noise.

Shot noise arises from the discretization of nature, e.g. when we consider the electricity as a stream of electrons or the light as a stream of photons. In particular, this kind of noise is related to the fluctuations in the number of particles, like the photons emitted by a light source. If the light source works at low intensity these fluctuations are higher while they get lower increasing the number of photons emitted.

However increasing the light power leads to another kind of noise called ra-

---

<sup>1</sup>Central limit theorem: the average of a large number  $n$  of independent measurements having a standard deviation of  $\Delta\sigma$  converge to a Gaussian distribution with standard deviation of  $\frac{\Delta\sigma}{\sqrt{n}}$

diation pressure noise which is related to the mirror motion that introduces a phase difference between the arms of an interferometer [3].

Both shot and radiation pressure noises get important at higher frequencies while, for example, at lower and intermediate audio-band frequencies the limitations to perform a precise measure come from seismic noise and suspension thermal noise, as we will see in the case of gravitational waves detection. Finally we should also take in account the technical noise of the apparatus, inefficiencies and losses.

From now on we will focus just in measurements perform with photons.

### 1.1.2 Fundamental Quantum Limit

Overcoming the SQL, and so improving the precision in a measurement process, is possible employing quantum techniques [4].

In quantum mechanics to each physical quantity, observable, is associated a specific mathematical operator. When a measurement is performed on two observables their operators are multiplied. In particular measure before  $\hat{A}$  and then  $\hat{B}$  correspond to multiply  $\hat{A}\hat{B}$ , viceversa is  $\hat{B}\hat{A}$ . The difference  $\hat{A}\hat{B} - \hat{B}\hat{A} = [\hat{A}, \hat{B}]$  is called commutator, if it is equal to zero it means that there is no difference in measure before one or the other. Otherwise, if  $\hat{A}$  and  $\hat{B}$  do not commute  $[\hat{A}, \hat{B}] = \hbar$ , where  $\hbar$  is the Planck constant, and it is said that the two observables are complementary.

We find this commutator in the Heisenberg uncertainty principle [5] which defines the fundamental limit:

$$\Delta\hat{A}\Delta\hat{B} \geq \frac{1}{2} | \langle [\hat{A}, \hat{B}] \rangle | \quad (1.2)$$

This principle states that it is impossible to measure two non-commuting properties of a quantum object simultaneously with infinite precision. Examples of these non-commuting couples are: momentum/position and time/energy [6]. On the other hand when two quantities commute,  $[\hat{A}, \hat{B}] = 0$ , it is possible to measure both simultaneously with the wanted accuracy.

This fundamental principle leads also, as a consequence, to the so-called

Heisenberg limit [7, 8]:

$$\Delta\varphi > \frac{1}{N} \quad (1.3)$$

With this limit there is an improvement of  $\sqrt{N}$  compared to the SQL but to get it is necessary to employ quantum states of light, such as squeezed states or entangled photons.

**Squeezed State** A squeezed quantum state is a kind of non-classical light state where the standard deviation of an observable (i.e. phase) is squeezed, while the one of another observable, which does not commute with this first (i.e. intensity), grows. It means:

$$\langle(\Delta\hat{A})^2\rangle < \frac{1}{2} |\langle\hat{C}\rangle| \quad (1.4)$$

$$\langle(\Delta\hat{B})^2\rangle > \frac{1}{2} |\langle\hat{C}\rangle| \quad (1.5)$$

where  $[\hat{A}, \hat{B}] = i\hat{C}$ . In this way the Heisenberg principle still holds but for one of the two observables is possible to get around it.

For instance, by fine-tuning the amplitude and phase quadratures it is possible to reduce the radiation pressure, squeezing the amplitude, which brings, at the same time, to an increment of the photon-counting noise, or vice-versa [9].

**Entanglement** Entanglement is a very peculiar quantum correlation between two or more indistinguishable quantum particles, which cannot be described independently even when they are separated by a large distance. As a consequence the central limit theorem does not hold anymore and so this correlation between components of the entangled state increases the precision in the estimation of a parameter [10].

Anyway, it is also important to know where to make use of these quantum states. A measurement process can be usually divided into three steps (fig.1.1): the preparation of a probe (photons in optical measurements), its interaction with the system to be measured and the probe readout. The first

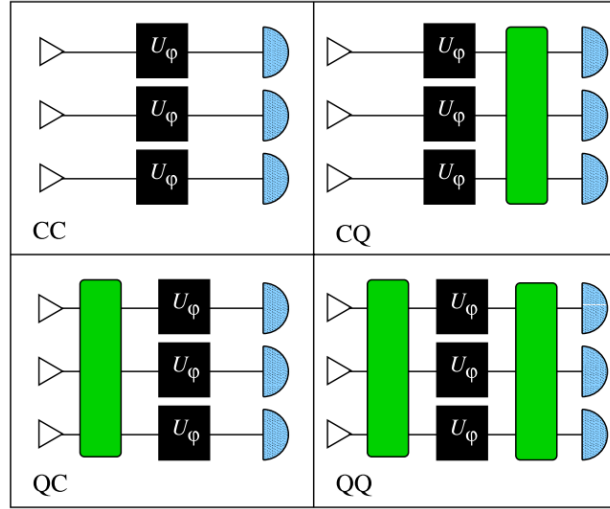


**Figure 1.1:** *Different strategies for the estimation of a parameter ( $C$ =Classical,  $Q$ =Quantum). For example  $QC$  means that a quantum strategy is employed in the preparation stage, while the detection is made classically. The black-boxes are the unitary transformations which describe the interaction probe-system. Image taken from [11].*

and third steps can be chosen to be either classical or quantum, but what is actually important is just the first, as showed in [11]. It is indeed only in the step of preparation that we have to adopt a quantum state (i.e. adopt entangled states), while at the measurement stage is useless to perform a quantum measurement.

In the second section of this chapter there will be some examples about this enhanced-parameter estimation which procedure is at the base of several kinds of interferometers, like the Mach-Zehnder and Ramsey.

### 1.1.3 Phase sensitivity, resolution and Fisher information

One of the main promises of quantum metrology is phase super-sensitivity, which is related to a decrement in phase uncertainty. In general the phase which gives this maximum sensitivity is not, trivially, the same of the phase at which the slope of the interference fringe is maximum, as proofed by Okamoto

*et al* [12]. On the other hand it has been demonstrated [13] that phase super-resolution, where for resolution is meant the number of interference oscillations in one cycle, can be achieved also through classical methods and, so, it is not a peculiar quantum feature.

Starting from these premises, Okamoto *et al* have defined the sensitivity  $S$  as  $S = (\sqrt{N}\Delta\varphi)^{-1}$ . Thus when  $S > 1$  SQL is beaten. Moreover, when the precision of the measurement reaches the Heisenberg limit,  $S = \sqrt{N}$ .

Another important parameter that is often mentioned in quantum metrology is the quantum Fisher information  $F$  of an estimated phase. The Fisher information is a way of measuring the amount of information that, in our case, a photon at the output carries about its phase. Maximize this information is also one central goal for metrology. For instance if a sample, usually in the biology field, risks to be damaged by an exposure to a strong beam, a high  $F$  decreases this need of exposure, maximizing the information gained using few photons [14].  $S^2$  can be interpreted as the Fisher information per photon since  $F = \frac{1}{\varphi^2}$ , as defined by the Cramer-Rao bound.

The estimation of quantum Fisher parameter has been carried on by Pang and Brun [15] who showed how it is always possible to reach the Heisenberg limit. Moreover they derived its value for a general Hamiltonian parameter, in particular of a spin -1/2 in a magnetic field.

#### 1.1.4 Limitations

By comparing SQL and Heisenberg limit, it is immediate to see that this latter scales  $\sqrt{N}$  faster but, on the other hand, there are also some limits in the employment of quantum methods.

The first general issue is related to the presence of technical noise (i.e.laser fluctuations, vibrations and so on) that can dominate on shot noise. In this case the achievable increasing in precision goes lost. Moreover, we have to take into account also the detector inefficiency, the absorption and transmission losses of the optical elements, which introduce statistical uncertainty, not so important for coherent classical measurements, but fundamental for the quantum ones.

Speaking about entanglement, the major limitation is found in the growing fragility of this kind of quantum states increasing the number of photons involved. For instance when a loss of a photon localizes the others the entanglement is completely erased. Moreover, although the generation of NOON states<sup>2</sup> with  $N=1$  or  $N=2$  can be done deterministically, this is not true for arbitrary  $N$ . Until now it has been generated NOON states until a maximum of 5 photons, using post selection, and 4, using ancillary-photon detection [16].

Squeezed states, instead, find their main limitations in the use of not ideal setups and, so, are mostly related to losses and inefficiencies. It is possible to conclude that, in general, squeezed states provide a better performance compared to entangled states [14].

## 1.2 Phase detection

In this second section we will explain better the improvement of phase detection in quantum metrology, focusing in particular on the Mach-Zehnder interferometer. More applications will be briefly presented in the last section.

### 1.2.1 Beam splitter: classical and quantum view

A beam splitter is an optical device in which the light enters from one, or both, input ports and it is split between the two output ports. For instance, with a 50:50 beam splitter, half of the input power exits from one output and half from the other. More technical details will be explained in Chapter 2, here we will focus just on the phase shift the light acquires impinging on the device. In particular, speaking about a beam splitter made by a glass plate with a dielectric coating on one side, the phase shift gained can be 0 or  $\pi$ . The reflected beam which impinges on the dielectric side will acquire a  $\pi$  shift, if instead it pass through the glass and then it arrives at the dielectric there will be no shift. The explanation is found in the Fresnel equations:

---

<sup>2</sup>NOON states are particular  $N$  particles entangled states which, as it will be explained in the following paragraphs, cover a central role in quantum metrology.



reflection causes a phase shift only when light passes from a lower refractive index to an higher one. The dielectric coating has a lower refractive index compared to the glass but, obviously, higher than the air. From here the two different phase shift.

In this previous description we have assumed that in the beam splitter enters only a light beam from one port. Different is the case taking into account also the vacuum fluctuations at the “unused” port, which is necessary to treat the beam splitter from a quantum mechanics point of view [17]. When a single photon impinges on the beam splitter it has 50% probability to be transmitted or reflected. This initial state can be written as  $|0\rangle|1\rangle$ , which means zero photons (vacuum) at one port and one photon at the other. Applying quantum mechanics calculations what we have after the beam splitter is:  $(i|1\rangle|0\rangle + |0\rangle|1\rangle)/\sqrt{2}$  where  $i$  is the imaginary unit related to the phase gained from the reflected photon. This last state is an entangled NOON state with  $N=1$ . In general a NOON state is written like:

$$|\psi\rangle = \frac{1}{\sqrt{2}}(|N\rangle_a|0\rangle_b + |0\rangle_a|N\rangle_b) \quad (1.6)$$

where we can have  $N$  photons in the spatial mode  $a$  and 0 in  $b$ , or vice versa, and, since they are entangled, the whole system can be described with a superposition of both possibilities. The understanding of how a beam splitter works is very important since they are basic components of an interferometer.

### 1.2.2 MZI: classical approach

The Mach-Zehnder interferometer (MZI) was proposed by the physicists Mach and Zehnder in the 1891 [18] and its setup is showed in figure 1.2.

The main goal of this instrument is to measure the difference in phase of two beams by measuring their interference. Depending on the phase  $\varphi$  acquired, the second beam splitter will reflect, with an efficiency between 0 and 100%, the beams which have traveled along the interferometer paths. Let us analyze it in more details [19].

The beam is injected from port A and the first beam splitter splits its am-

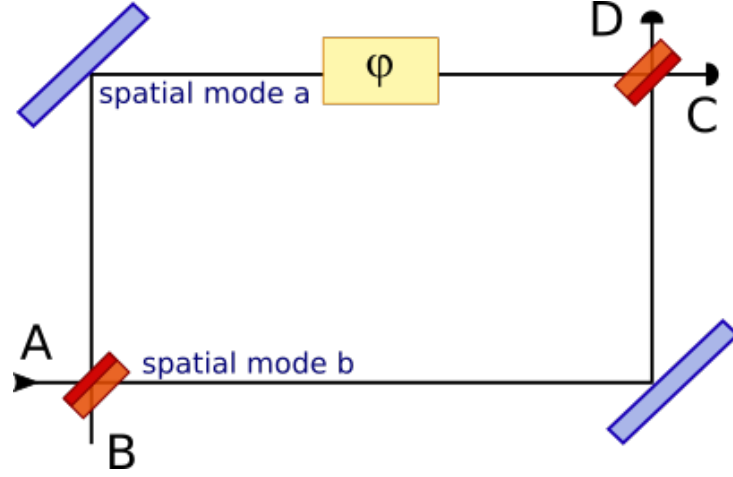


**Figure 1.2:** Mach-Zehnder interferometer. It is constituted by 2 beam splitters (orange) and two mirrors (blue). In one of the two arms it is present a phase shifter in order to put an additive phase  $\varphi$ . The light beam enters from input port A and is collected at the output C and D.

plitude 50% to each arm. According to what explained in the previous paragraph, the beam on the reflected mode (spatial mode a, fig.1.2) will gain an extra phase of  $\pi$  with respect to the transmitted one. Thus at the entrance to the second beam splitter the light in the spatial mode a has gained a phase of  $2\pi$  while in spatial mode b only  $\pi$ . Moreover the phase depends also on the optical path traveled  $L$  which adds a contribution of  $\frac{2\pi L}{\lambda}$ .

The second beam splitter is arranged in order to have the dielectric surface on the right-hand side. So, as state by the Fresnel law, due to the reflection from an higher reflective index (glass) to a lower one (dielectric), there is no a phase gain of  $\pi$  this time. Thus, after the second beam splitter, on the way of detector D the phase of the upper path is:

$$2\pi + 2\pi \left( \frac{L1 + l}{\lambda} \right) \quad (1.7)$$

where  $L1$  is the distance traveled along the path of spatial mode a and  $l$  the one inside the beam splitter. The same reasoning is valid for the path of

spatial mode b and making the difference between these two we obtain:

$$2\pi + 2\pi \left( \frac{L1 + l}{\lambda} \right) - (\pi + 2\pi \left( \frac{L2 + l}{\lambda} \right)) = \pi + 2\pi \left( \frac{L1 - L2}{\lambda} \right) = \pi + \varphi \quad (1.8)$$

where  $\varphi$  is the phase difference due to the possible different length of the two paths L1 and L2.

At detector C instead the light in spatial mode b acquires an additive phase of  $\pi$  so that the final one is:

$$2\pi + 2\pi \left( \frac{L1 + 2l}{\lambda} \right) - (2\pi + 2\pi \left( \frac{L2 + 2l}{\lambda} \right)) = \varphi \quad (1.9)$$

Finally we can conclude that if there is no phase gain  $\varphi$  along the arms we have a constructive interference at the output C and a destructive one at output D. Otherwise tuning the value  $\varphi$  we reach all the intermediate situations described by these equations:

$$I_C = \cos^2(\varphi/2) = \frac{1}{2}(1 + \cos\varphi) \quad (1.10)$$

$$I_D = \sin^2(\varphi/2) = \frac{1}{2}(1 - \cos\varphi) \quad (1.11)$$

where  $I$  is the normalized intensity measured at the outputs C and D with an error  $\Delta\varphi$  proportional to the SQL  $1/\sqrt{N}$  as explained in the previous paragraphs.

### 1.2.3 MZI: single photon interference

We have just explained how a Mach-Zehnder interferometer works with classical light. However the situation changes if, as input, we use a single photon and we pass through quantum mechanics [17].

Assume as input state  $|0\rangle|1\rangle$  (so one photon at port A and none at port B) with the first beam splitter we have the following transformation, as already mention in paragraph 1.2.1:

$$|0\rangle|1\rangle \longrightarrow \frac{1}{\sqrt{2}}(|1\rangle_b|0\rangle_a + i|0\rangle_b|1\rangle_a) \quad (1.12)$$

that is an entangled state, the photon can be in both arms and we do not know in which it actually is [20]. Then, with the phase shifter the photon in mode a (fig.1.2) acquires an additive term of  $e^{i\varphi}$ .

At the second beam splitter the entangle state undergoes again at the beam splitter transformation and what we get at the output is:

$$|\psi_{fin}\rangle = \frac{1}{2}(|0\rangle_b|1\rangle_a(1 - e^{i\varphi}) + i|1\rangle_b|0\rangle_a(1 + e^{i\varphi})) \quad (1.13)$$

Performing the square modulus of each term we end with the probability to detect a photon at output C:

$$P_C = |\langle 1|\langle 0|\psi_{fin}\rangle|^2 = \frac{1}{2}(1 - \cos\varphi) \quad (1.14)$$

While the probability to detect a photon at output D is:

$$P_D = \frac{1}{2}(1 + \cos\varphi) \quad (1.15)$$

These probabilities are the same we get classically. Instead, the fact we can have interference with just one photon is explained just quantum mechanically and it is due to the lack of "which path" information. Indeed, we do not know which path the single photon has taken since it is in a superposition of both possibilities and that is why interference appears.

In conclusion, in this application we do not see an improvement in the measurement since, in this case, the SQL and Heisenberg limits are equivalent with the employment of a NOON state with  $N=1$ . Thus we will proceed in the next paragraphs increasing the number  $N$  of photons used, looking at the consequences.

#### 1.2.4 Improvement with NOON state ( $N=2$ )

Now we will explore what happens injecting  $N=2$  photons, one per input port. Always adopting quantum mechanics to do the calculation, after the

first beam splitter we get [17]:

$$|\psi\rangle = \frac{i}{\sqrt{2}}(|2\rangle_b|0\rangle_a + |0\rangle_b|2\rangle_a) \quad (1.16)$$

Thus we always have both the photons in the same arm, even if we do not know in which. The absent output  $|1\rangle|1\rangle$  corresponds to the situation of both photons transmitted or reflected and these processes are indistinguishable. In order to explain this fact it is possible to re-call Feynman's rule: the probability for an outcome is given by the sum of the probability amplitudes of all the indistinguishable processes and then calculate the square modulus. The result, keeping in mind that a reflection brings to a phase of shift, is zero. The experimental demonstration was made by Hong, Ou and Mandel [21], which is also useful to check if a process generates indistinguishable photons. It is also important to point out that this is not a general result, with N photons at each input port we will not get a NOON state but more calculations are necessary.

Let us use now the NOON state with N=2, generated with the first beam splitter of a Mach-Zehnder interferometer, where is always placed a phase shifter in one of the two arms. Like in the case of one photon the photons in that arm acquire a phase:  $\frac{i}{\sqrt{2}}(|2\rangle|0\rangle + e^{i2\varphi}|0\rangle|2\rangle)$  after the second beam splitter what we get is:

$$|\psi_{fin}\rangle = \frac{1}{2\sqrt{2}}(1 - e^{i2\varphi})(|2\rangle_b|0\rangle_a - |0\rangle_b|2\rangle_a) + \frac{i}{2}(1 + e^{i2\varphi})|1\rangle_b|1\rangle_a \quad (1.17)$$

In order to measure the phase it is useless to measure the average photon number at the detector, as before, since both arms give the same result. It is necessary instead to measure the parity (evenness or oddness of the photon numbers) of one of the two beams [8]. The final result we get, projecting the final state (eq.1.17) as we did in eq.1.14, is  $\cos(2\varphi)$ , so a function which oscillates at the double of the case N=1 [17], from here we have directly the super-resolution. Following the calculus of the error propagation we finally obtain a standard deviation of the phase of  $1/2$  instead of  $1/\sqrt{2}$ . We can conclude that, in theory, using an entangled state we reach the Heisenberg

limit overcoming the SQL.

### 1.2.5 General improvement employing NOON state

The result presented in the previous paragraph can be put in more general terms.

We take as initial state the NOON entangled state  $\Psi_{in} = (|N\rangle|0\rangle + |0\rangle|N\rangle)/\sqrt{2}$ . It interacts with the system, undergoing a phase shifting unitary transformation  $U_\varphi = e^{i\varphi\hat{n}}$ , where  $\hat{n}$  is the photon number operator<sup>3</sup>, the result is [14]:

$$U_\varphi|N\rangle = \sum_{j=1}^{\infty} \frac{(i\varphi\hat{n})^j}{j!} |N\rangle = e^{i\varphi N} |N\rangle \quad (1.18)$$

Thus the NOON states acquire an N-amplified phase shift and, from that, the enhancement in precision at the detection stage and the intrinsic super-resolution due to this N-faster oscillations [22].

A coherent light source (i.e. a laser) is, instead, described by a coherent state  $|\alpha\rangle$  whose amplitude is connected to the mean photon number by  $|\alpha|^2 = \langle\hat{n}\rangle$ . Applying  $U_\varphi$  to this coherent state:

$$U_\varphi|\alpha\rangle = e^{-|\alpha|^2/2} \sum_{j=1}^{\infty} \frac{(e^{i\varphi}\alpha)^j}{\sqrt{j!}} |j\rangle = e^{i\varphi} |\alpha\rangle \quad (1.19)$$

so the final result does not bring any amplification of the phase and, so, any improvement in the detection of it. From here the need to repeat the measurement  $N$  times and apply the central limit theorem. Moreover, always applying the error propagation theory, the results lead us to the SQL or Heisenberg limit, depending on the preparation stage we start, quantum or classical.

---

<sup>3</sup>The photon number operator is related to the number of energy quanta excited in a state:  $\hat{n}|n\rangle = n|n\rangle$  where  $|n\rangle$  is the photon number state and  $n$  the photons excited in the state  $|n\rangle$  from the vacuum state.

### 1.2.6 Multiparameter estimation

Another important subject of interest is the possibility to perform multiparameter phase estimation. In order to achieve that multiport devices are used, such as three- or four-port beam splitters (called tritters or quarters). A tritter (quarter) is a device which splits a beam in three (four) parts instead of just two, like a normal beam splitter. If a splitter is named symmetric it means the beam is divided into equal parts at the output. A more detailed explanation will be given in the next chapters.

A three-arm interferometer is obtained putting in sequence two symmetric tritters and it is possible to estimate until two phases simultaneously, respect to a reference. This estimation can be achieved thanks to an adaptive protocol like the one used by Spagnolo *et al* [23]. Moreover also the amount of Fisher information of the phase can be extracted and checked if the classical limit it is overcome or not.

## 1.3 Applications

In this last section are reported examples of several quantum technologies in which the quantum-enhanced parameter estimation has found application [4].

### 1.3.1 Quantum biology

In the field of quantum biology is important to be able to observe a certain tissue or structure respect to the surrounding others, without damaging it. This damage can come from heating or photochemical effects [14]. In the first case the damage is strongly correlated with the presence of water and, so, with its high absorption in the infrared area. On the opposite photochemical effects (such as dissociation of molecules) get worst with the decreasing of wavelength, since it means an increase of the energy. These are two more constraints that have to be taken in account in order to apply imaging techniques in this study area.

Anyway, employ quantum metrology methods in biology let to achieve the

same or better precision in the study of a sample, decreasing the light exposure, and so the possible damages. For instance in two-photons microscopy, in order to get a good fluorescence, it is required to use high intensity beam. On the other hand, with entangled photons, is possible to perform measurement on light-sensitive samples getting around this problem and so, for example, measure the protein concentration in a solution, as explained in the work of Crespi *et al.* [24].

Crespi *et al.* fabricated, always by FLM techniques, a Mach-Zehnder interferometer coupled with a microfluidic channel passing through one of its arm. In this channel flows a light-sensitive solution and a phase shift, induced by the concentration-dependent refractive index, is acquired by the photons which travel inside the interferometer. Thus, depending on the concentration of a certain protein inside the solution, a different pattern of the interference fringes is detected. In this work it is proofed, employing entangled photons, the overcoming of SQL and the achievement of super-resolution.

### 1.3.2 Quantum imaging

Imaging protocols regard many different aspects: microscopy, spectroscopy, lithography, etc. We start with one of the most famous quantum imaging experiment: the reconstruction of a ghost image.

A ghost image is the image of an object produced without directly looking at it. Thus there are two paths (fig.1.3), in one there is the object while in the other nothing, at the end of each path there is a detector. The photon in the first path can be absorbed or not by the object and so can be detected or not by the corresponding detector (called bucket because without spatial resolution). The correlated-photon following the second path will reach its camera and, looking at the coincidences with the first photon, absorbed or not, the image of the object can be reconstructed. This procedure has classic nature, either if we use entangled photons or correlated light beams. The quantum nature lies in the fact that both near and far-field plane can be perfectly imaged with the same apparatus using entangled photons and in the creation of noiseless images [4].



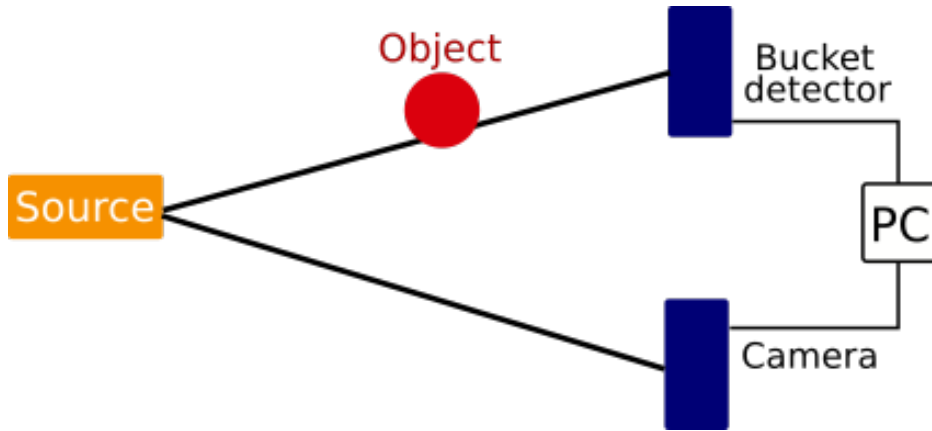


**Figure 1.3:** *Schematic setup for the reconstruction of a ghost image. The object to reconstruct is on the path of a bucket detector (no spatial resolution), while the image reconstruction is made combining the information collected from bucket detector and camera.*

For what concern lithography and two-photon microscopy the biggest limitation lies in the Rayleigh criterion<sup>4</sup> which defines the bound to resolve two points. Considering the diffraction through a slit the angular resolution  $\theta_R$  is  $\sin\theta_R = \frac{\lambda}{d}$  where  $\lambda$  is the wavelength of the light passing through the slit and  $d$  the width of the slit. Thus decreasing  $\lambda$  the resolution gets higher but it is not possible to go below a certain wavelength, since this would increase also the energy of the radiation. Thanks to entangled photons, especially NOON states, it is possible to overcome this limit. Keeping the wavelength of the radiation field constant the one of the NOON state is  $\lambda/N$  with an increasing in resolution [4].

### 1.3.3 Quantum frequency

In this application, typical for spectroscopy, the phase factor which is going to be measured is time-dependent and equal to  $\varphi = \omega t$  where we are interested in estimate the time  $t$ , related to the life time of th atomic state, or frequency  $\omega$  of an atomic transition [8, 25]. In order to accomplish this it is used a Ramsey interferometer [26] which is formally equivalent to a MZI but the

---

<sup>4</sup>Rayleigh criterion: two point sources are regarded as just resolved when the principal diffraction maximum of one image coincides with the first minimum of the other.

entanglement, in this case, is made by a superposition of two atomic states instead of two photons. It is indeed an atomic interferometry based on the phenomenon of magnetic resonance, it is also used in the S.I. for the definition of the second.

We say that a system is in magnetic resonance when its natural frequency  $\omega_0$  is equal to the frequency used to interact with it, like applying an external oscillating electromagnetic field  $\omega$ . The probability to transfer an atom from its excited to its ground state is maximum when the detuning  $\Delta = \omega - \omega_0$  is equal to 0, so when it is in magnetic resonance.

Thus our entangled state this time will be the superposition of the ground state  $|0\rangle$  and the excited state  $|1\rangle$  for each ion:  $(|0\rangle + |1\rangle)/\sqrt{2}$ . These ions are indeed independently excited by an electromagnetic field, which acts like the first beam splitter of MZI, and then undergoes to a free evolution for a time  $t$  which introduces a phase factor between the two states. Applying another, identical electromagnetic pulse and measuring the probability to be in state  $|0\rangle$  is possible to retrieve this phase. Anyway, in order to overcome the SQL, it is necessary to build at the beginning an entanglement of all  $N$  ions otherwise, even repeating the measure  $N$  times, the maximum accuracy will be always limited by the expression 1.1.

### 1.3.4 Quantum positioning and clock synchronization

**Positioning** A way to find the position of an object is to measure the time of arrival of a light beam which travels from that object to a known reference point. Classically this means to average the time-travel of the single photons in the beam. The error is so proportional to  $1/(\Delta\omega\sqrt{N})$  where  $\Delta\omega$  is the bandwidth of the signal. The minimum time duration detectable, closing related to the accuracy of the position, is  $1/\Delta\omega$  per each photon, thus it depends on the spectral distribution of the signal.

Even in this case, thanks to quantum strategies, is possible to improve the result. Especially entangling  $N$  photons in frequency each of them will have the same bandwidth  $\Delta\omega$  leading to the usual improvement of  $\sqrt{N}$  [27].

Other limitations that have to be taken in account in order to measure the

position are related to the power of the beam because of the losses and its broadening due to the possible transit in dispersive media. This last is even overcome exploiting quantum techniques [28].

**Clock synchronization** The problem of synchronize distant clocks is closely correlated to the one of positioning. The most common protocols used are the Einstein synchronization and the Eddington's slow clock transportation. The first procedure is based on exchange of light pulses from one clock to another, in the second the two clocks are synchronized locally and then, one of the two, is transported infinitesimally slowly (adiabatically) to its final location.

As mentioned in 1.3.3 atomic clocks are based on Ramsey's method since the measure of time (or frequency) is connected to the transition of electrons between energy levels. The accuracy of the clock depends indeed on the frequency and width of the electronic transition: higher frequencies and narrow bandwidth improve the precision. In addition one of the main limitations to the precision of atomic clocks is due to atomic quantum noise, originating from Heisenberg uncertainty principle. It is to overcome this that quantum states are necessary to be employed.

For instance it is possible to use entangled state however, in this case, it is necessary to take into account also the presence of decoherence since it strongly limits the performance [29].

### 1.3.5 Gravitational waves detection

Gravitational waves are predicted by Einstein's general theory of relativity as curvatures of spacetime which propagate as waves. The Laser Interferometer Gravitational-Wave Observatory (LIGO) Project has the aim to detect them. In order to do that are used Michelson-type kilometer-scale interferometers with mirrors suspended in vacuum. The frequency of gravitational waves goes from few Hz to some kHz but vacuum fluctuations and other noise limits the sensibility to few hundreds of Hz (fig. 1.4). To overcome this squeezed states are employed so that the noise is not more equally distributed in the

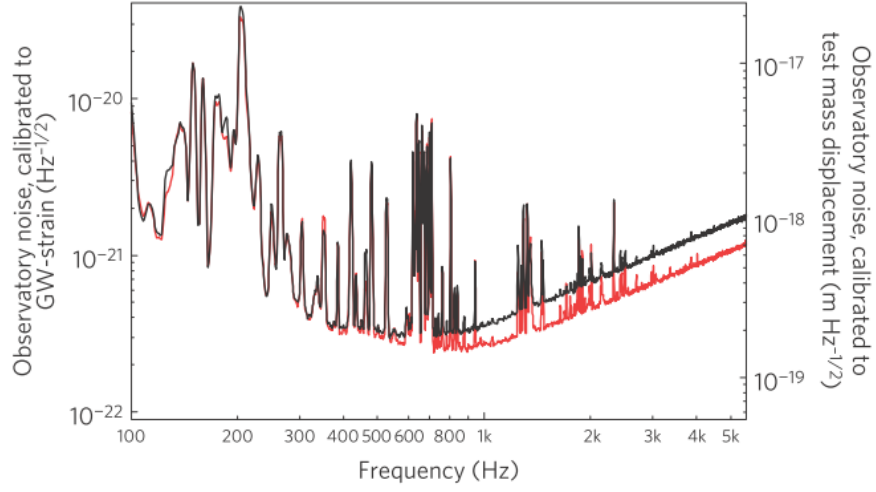


**Figure 1.4:** *In the shot noise frequency limited band (above 700Hz) there is a reduction of the noise (red trace) thanks to the injection of squeezed states. At lower frequency instead the limitations is given to the insufficient seismic isolation of the mirrors. Image taken from [30].*

quadratures, in particular the phase-quadrature is squeezed such that the measure of it is more accurate. Moreover in the observatory's apparatus are present also filters to eliminate other sources of noise [30].

This application is the first that is actually practical for squeezed states, even though they are an important components also in experiments such as quantum teleportation or quantum memories.

## Chapter 2

# Femtosecond Laser Micromachining

In this chapter it is firstly explained the physics behind waveguides writing technique of Femtosecond Laser Micromachining (FLM).

In the second section the most important parameters, from which the fabrication process depends, are reported.

In the last section are showed some relevant devices fabricated by FLM.

## 2.1 Introduction

There are many techniques ideated for fabricating photonics circuits; the one we are interested in is Femtosecond Laser Micromachining (FLM) useful for writing optical waveguides in transparent materials. This method was born from a work of Davis *et al* [31] in 1996 and it is based on non-linear absorption of focused ultrashort laser pulses which induce a local and permanent modification in the dielectric substrate.

In the following section we will explain in more details how this non-linear absorption process works and the different parameters that can be tuned in order to achieve the wanted smooth refractive index change and circuit geometry.

With respect to lithography FLM offers advantages:

- it is a maskless and single-step process, which requires a relatively simple setup and does not require the use of special facilities such as clean rooms. This bring to a consistent cost reduction and process speed-up, very useful for prototyping of new designs on small scale production;
- it is flexible since it is adequated to fabricate in different materials (glasses, crystals, polymers) just adjusting the laser radiation parameters, without changing the process;
- thanks to the non-linear nature of the light-matter interaction process of FLM, the material modification is highly localized at the beam focal spot. This permits to fabricate the waveguides with a 3D geometry, and to develop circuit designs with configurations otherwise impossible to get.

### 2.1.1 Femtosecond laser interaction

Linear absorption of light at frequency  $\omega$  takes place in a certain material when the energy carried by a photon is higher than the material band gap

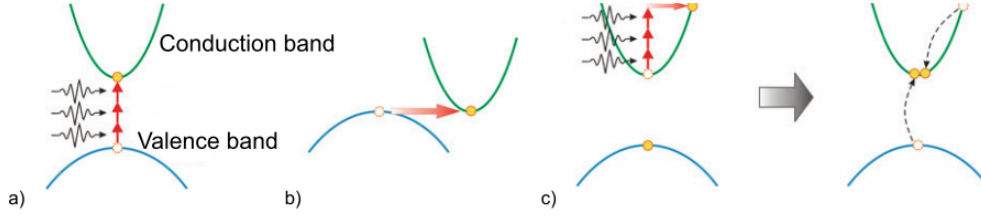


**Figure 2.1:** *Non-linear light absorption processes: (a) multiphoton absorption; (b) tunneling; (c) avalanche ionization. Image taken from [32].*

$E_g$ :  $\hbar\omega \geq E_g$ . In FLM we want to avoid this linear absorption, thus the material must be transparent at the fabrication wavelength. The reason why non-linear absorption is essential lies in the fact that it lets to obtain a permanent and localize modification in the substrate since it induces only in the focal region of the beam, due to the very high peak intensity required. Non-linear absorption can be of different kinds: multiphoton absorption, tunneling and avalanche ionization (fig.2.1). These processes are at the basis of the generation of free electron plasma to which follows energy relaxation and material modification.

Multiphoton absorption consists in the simultaneous absorption of  $n$  photons from a valence electron such that  $n\hbar\omega \geq E_g$ . This happens when the laser intensity is relatively low and brings the electron to the conduction band.

With higher electric field, instead, there is a deformation of the conduction and valence bands, leading to a lowering of the potential barrier, so that electrons can flow from the latter to the first one thanks to a tunneling effect.

These two processes coexist during the laser exposure, and their result is the same: the promotion of electrons from the valence to the conduction band. They actually do not depend only from the intensity of the light, but also on the effective mass of electrons and laser frequency.

This seed of free electrons in the conduction band can linearly absorb other photons from the same laser pulse, increasing their kinetic energy and this can lead, by impact ionization, the promotion of other electrons from the valence to the conduction band. This process is called avalanche ionization and gives, as a consequence, the formation of a hot plasma of free carriers,

which grows in density until the laser pulse is present. When the laser pulse is finished, this plasma relaxes and it releases its energy to the surrounding lattice of the material, which is deformed, leading to a change of its properties. Depending on the energy of the pulse, we can have three different kinds of modification, as we will explain in the next paragraph.

The sub-picosecond pulse duration is an essential ingredient in FLM, mainly for two distinct reasons. The first one is that the absorbed energy is transferred to the lattice in the order of picosecond time-scale and thus it is decoupled respect to the non-linear absorption processes.

The second one is related to the fact that multiphoton and tunneling ionization need high peak intensity to be triggered in a deterministic fashion, leading to the promotion of electrons which will induce the avalanche ionization. It is also true that this seed of free electrons can also be produced thermally or by the presence of impurity and defect states. The problem is that, in this latter case, the plasma density will be lower and it will fluctuate, bringing to a stochastic breakdown with strong repercussions on the uniformity and the quality of the modification.

It is necessary to point out that, anyway, the precise mechanism and reasons which lead to a change in the refractive index are still not completely clear since many phenomena occur together during the plasma relaxation, such as ion exchange/migration [33], color center formation [34] and densification [35].

## 2.2 Fabrication parameters

### 2.2.1 Pulse energy and translation speed

As already mentioned above, depending on the femtosecond pulse energy, we can end up with three different effects induced in the material.

In particular pulses at low intensities produce, in the focusing volume inside the substrate, a smooth and isotropic change of refractive index, that, for suitable irradiation parameters, can be positive. This regime is the one in which we are more interest in for waveguide writing [36, 37].



Instead, with slightly higher intensities, the refractive index changes more abruptly leading to birefringent structures. This birefringence can be exploited in some applications, for example in devices where a polarization spatial dependence is useful.

Rising further the intensity causes the generation of micro-explosions inside the material due to shock waves and this leads to the formation of cracks and micro-voids inside the material. This case is of interest for some applications which generally do not have waveguiding properties but, for instance, are useful for three-dimensional data storage. This is the case of microvoids representing voxels (volume pixels) [38].

The final refractive index profile produced in the material by FLM also depends from the amount of total energy deposited per unit volume and this is controlled by the translation speed. Obviously, the higher is the speed, the less is the energy per unit volume deposited. It is also important to notice that, given the non-linearity of the process, there is no equivalence in the increasing (lowering) of translation speed with the same energy pulse and the lowering (increasing) of pulse energy at constant speed.

### 2.2.2 Repetition rate

Another crucial parameter in waveguide writing by FLM is the repetition rate of the laser pulses. We can individuate three different regimes [39].

At low repetition rate (less than 100 kHz) two consecutive pulses arrive after the complete cool down of the substrate, since the heat released by the first pulse is already completely dissipated. This is the so-called single pulse modification regime. It leads to less uniform waveguides and accumulation of birefringent stress, in addition to a low fabrication speed.

Increasing the repetition rate up to several MHz we have a completely different situation. The heat cannot diffuse between two consecutive pulses and, so, there is a strong heat accumulation at the focal point. The temperatures reached in the material during the fabrication in this regime are then much higher than in the previous regime, and this causes a partial melting of the substrate and its consequent re-solidification. As demonstrated by Eaton and

co-workers [40], this regime is ideal for the waveguide inscription in borosilicate glasses, where it is possible to obtain very uniform and less asymmetric waveguides, which exhibit reduced birefringence and a more circular guided mode, with benefits both on propagation losses and coupling losses to optical fiber. Finally, in this regime, there is also a speed up of the overall fabrication process, up to 50-100  $mm/s$ , instead of tens of  $\mu m/s$  like in the previous regime.

There is then also an intermediate regime, from hundreds of kHz to few MHz. In this case is not required, like in the second regime, a tight focusing and long working distance objectives can be employed so that it is possible to exploit at maximum the 3D capabilities of FLM. Moreover, as for the latter regime, symmetric and uniform waveguides are generated allowing also to a good fabrication process speed.

### 2.2.3 Focusing conditions

In order to focus the femtosecond pulses into the substrate and trigger in the focal spot the non-linear absorption process, it is required an suitable system of optical elements system of optics. The standard choice is a microscope objective, which compensate both the spherical and the chromatic aberrations that would cause deviation in the intensity distribution of the focus.

The spatial intensity profile of the focused pulse, in the approximation of linear propagation and and null spherical aberrations, can be represented by a Gaussian beam. In this case the diffraction limited minimum waist radius  $w_0$  and the Rayleigh range<sup>1</sup>  $z_0$ :

$$w_0 = \frac{M^2 \lambda}{NA\pi} \quad (2.1)$$

$$z_0 = \frac{nM^2 \lambda}{NA^2\pi} \quad (2.2)$$

where  $M^2$  is the beam quality factor,  $\lambda$  the laser free space wavelength,  $n$  the refractive index of the material and NA the numerical aperture of the

---

<sup>1</sup>It is the distance along the propagation direction of a light beam from the waist to the position where the area of the cross section is doubled

focusing lens.

This last parameter is one of the most important, since it determines the size of the focal volume, which is tighter with higher value of NA, as it is obvious looking at the equations above (eq.2.2). On the other hand, increasing too much the value of NA is counter-productive in terms of the depth of the focus, which is another key parameter. In fact, the index mismatch at air/glass interface adds another contribution in spherical aberrations, an effect that is more relevant for higher NA values. A way to limit this effect is the employment of an oil-immersion objective, in order to quench the index mismatch or using an objective with variable depth aberration compensation.

Finally, another factor which has to be considered is whether the material under processing exhibits a significant value of non-linear  $n_2$  refractive index. Indeed, the propagation of a focused and intense ultrashort pulse in a highly non-linear material can give rise to some undesirable non-linear effects, that will further distort the focal spot. In particular this happens if the peak power exceeds the critical power for self focusing:

$$P_c = \frac{3 \cdot 77 \lambda^2}{8 \pi n_0 n_2}. \quad (2.3)$$

In this case the pulse collapses to a focal point and free electron plasma is generated. The latter behaves as a diverging lens balancing the Kerr-lens self-focusing leading to a distorted focal spot. These effects can become very relevant when long focal depths are used, and this may limit the applicability of FLM.

## 2.3 Photonic devices

In this section we will speak about some photonic devices fabricated by FLM. In particular we will focus our attention on devices fabricated in aluminum-borosilicate glass substrates, as they are more relevant for the development of this thesis work. We cite two studies about this type material, the first one by Eaton's group [40] which shows that high repetition rate (around 1.5 MHz) and high translation speed (some tens of mm/s) allow to fabricate

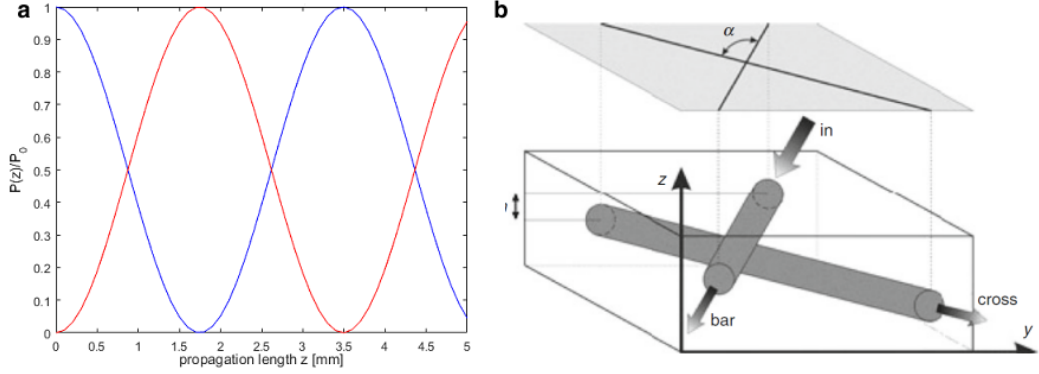


**Figure 2.2:** (a) Power exchange of a directional coupler with coupling coefficient  $k = 0.9\text{mm}^{-1}$ . Depending on the propagation length it is possible to choose the splitting ratio. The red and blue curves represent the power exchange from one waveguide to the other, when they cross a 50% splitting has been achieved. (b) Schematic of a X coupler. Image taken from [42]

with waveguide with high performances at telecom wavelengths ( $1550\ \mu\text{m}$ ). In particular, they demonstrated propagation losses of about  $0.3\ \text{dB/cm}$  and mode size of around  $10\ \mu\text{m} \times 10\ \mu\text{m}$ .

Another study was made by Sansoni *et al* [41] for waveguides at  $800\text{nm}$ . In this work, the authors have shown that waveguides fabricate in borosilicate glasses show relatively low bending losses, with values around  $0.3\ \text{dB/cm}$  for curving radius of  $30\ \text{mm}$ . In this case the reported propagation losses are of  $0.5\ \text{dB/cm}$  and a  $8\ \mu\text{m} \times 8\ \mu\text{m}$  mode field diameter.

### 2.3.1 Directional couplers

A directional coupler is an integrated optics device in which two waveguides get close and, in that region, a light power exchange, due to evanescent coupling, takes place. This phenomenon can be modeled in terms of coupled mode equations, as fully explained in [43]. In these equations one of the most significant term is the coupling coefficient  $k$ , which describes the overlap between the modes of the waveguides. It is related to the distance  $d$  of the two waveguides at the coupling region by:

$$k = Ae^{bd} \quad (2.4)$$

where  $A$  and  $b$  are constants, always related to the specific coupling.

The solution, in the hypothesis of symmetrical and identical waveguides, of the coupled mode equations is a modulated power exchange, like the one showed in figure 2.2a, which can be mathematically written as  $P_{exc} = \sin^2(kL)$ , where  $L$  is the length of the coupling region. Thus, from the choice of this length, it is possible to decide the amount of exchanged power and, so, the reflectivity  $R$  and transmissivity  $T$ , defined as:

$$R = \frac{P_{WG1in}}{P_{WG1out}} \quad (2.5)$$

$$T = \frac{P_{WG1in}}{P_{WG2out}}. \quad (2.6)$$

This means that the reflectivity is the amount of light power which remains in the first waveguide after the coupling, while the transmissivity is the power that crosses to the second.

Thus even a slight difference or imperfection in the writing of these waveguides leads to visible consequences in the performances of the device. For this reason, directional coupler fabrication is a benchmark for the success or not in the employment of FLM technique.

The first reported FLM direction couplers were made in borosilicate glasses realized in 2001 [44] working at 633 nm. They had an asymmetric geometry composed by a straight guide and a curved flanked one.

Another kind of coupler geometry is the X-coupler demonstrated by Osellame *et al* in 2005 [42]. As it is possible to see in fig. 2.2b, in this case the two waveguides are at two different depths and the splitting ratio is determined by the distance  $h$  and the angle  $\alpha$ .

The splitting ratio depends also on the wavelength and the polarization. The first dependence can be useful for some applications such as multi and demultiplexers while for others is a limitation that can be overcome by correctly choosing the geometric parameters in the design [45].

Even polarization dependence can be exploited in some technologies (i.e. polarization sensitive devices) or avoid in others where it is prejudicial [46].

**Beam splitter** A directional coupler is a beam splitter in its integrated circuit version. In particular, by performing an accurate choice of the coupling length it is possible to achieve a 50:50 splitting ratio.

### 2.3.2 Tritter

A tritter is a multi port beam splitter which splits a light beam in three different spatial modes instead of just two. It is called symmetric or balanced when an input photon has the same probability to exit through any of the three output ports. Theoretically the description of a symmetric tritter is made by a  $3 \times 3$  unitary matrix [47] assuming that the majority of the losses occur outside the chip:

$$U = \frac{1}{\sqrt{3}} \begin{pmatrix} 1 & 1 & 1 \\ 1 & e^{i2/3\pi} & e^{i4/3\pi} \\ 1 & e^{i4/3\pi} & e^{i8/3\pi} \end{pmatrix} \quad (2.7)$$

Different geometries are possible to fabricate this device.

In 1997 Marek *et al* [47] proposed a tritter made putting in cascade several two port beam splitters and phase shifters according to the geometry shown in figure 2.3a [48]. Anyway a device made with these bulk elements suffers of mechanical instabilities, especially when it is used as a component of a larger device, like multiport interferometers. It is possible to reproduce this decomposition approach in its integrated version [49] overcoming these problems.

Another possible geometry for realizing an integrated tritter was presented for the first time in [50] and fully exploits the 3D capability of FLM. It is a directional coupler made by three waveguides approaching each other to get a common coupling region (fig. 2.3b). Accurately choosing the coupling length respect to the distance is possible to achieve a balanced splitting.

Other similar 3D geometries are possible such as the one used in [51] where we have always three waveguides getting closer. In this case the geometry at the coupling region is isosceles while, in other works [52] was thought equilateral and then optimized to compensate non-idealities.

This last geometry was employed to accomplish a three photons interaction

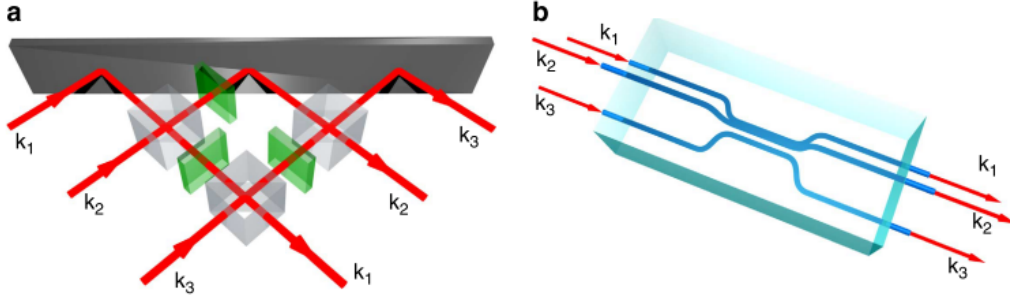


**Figure 2.3:** Schematic of a tritter. (a) Tritter as cascade of two port beam splitters, gray blocks, and phase shifters, green blocks. (b) Three dimensional tritter. Images taken from [52]

by evanescent field coupling without a decomposition into a cascade of components, difficult to control, providing a more compact device. In particular it has been used in the work of Spagnolo *et al* [52] to obtain three photons interference.

### 2.3.3 Mach Zehnder and multi-port interferometers

As already mentioned in the first chapter, a Mach Zehnder interferometer is a device composed by a first coupler which divides a light beam in two (or more, in case of multi port interferometer) different optical paths, which are then recombined at the output by another coupler. Depending on the difference of the phase shifts that light acquires on the different spatial modes inside the interferometer, interference fringes are observed at the device output ports. This phase shift difference can be originated by a geometrical imbalance of the light paths or by a local change in the refractive index in one or more spatial modes. Note that the phase shift can be also dynamically driven with a thermo-optic resistor.

The first fabrication of a MZI with FLM was made in 2002 by Minoshima *et al* [53] putting in cascade two X couplers. It works as wavelength filter thanks to a geometrically unbalanced design. The transmission spectrum detected shows a periodicity which fits for a  $9.3 \mu\text{m}$  path unbalance, quite in good agreement with the  $10 \mu\text{m}$  expected.

This last result was a good accomplishment, since even small imperfections

or variations in the design are enough to shift the interference fringes with respect to what was theoretically expected. One interesting example regarding this aspect can be the work of Florea and Winick [54] who tuned the device in real time by focusing femtosecond pulses on one branch until they reached the desired interference pattern.

Speaking about multi-ports interferometer even in this case we have several examples. For instance there is the work of Chaboyer *et al* [55] which developed a 3D geometry of a three-arm interferometer putting in cascade two 3D-tritters. In particular, one of its arms was fabricated very close to the sample upper surface and a thermo-optics phase shifter was fabricated on top of it. This allowed to dynamically tune the interference pattern produced at the interferometer output. Another three-dimensional interferometer [23] is depicted in fig.2.4a. The only difference with the previous is that there is no rising of the central arm.

Another way to build up a multi-port interferometer is decomposing it into more basic components, such as directional couplers and phase shifters [47]. For instance in the work of Crespi *et al* [56] a 5-arms interferometer was made with a network of these elements (fig.2.4b). The main challenge was to get the independent control of the 10 transmissivities and 15 phase shifters just by tuning the geometrical features of the device. However, the high degree of flexibility of FLM helped in order to reach the correct optical length for the induced phase shift and, at the same time, the wanted splitting ratio which depends on the distance of the two waveguides in the coupling region besides the coupling length.

### 2.3.4 Thermo-optic phase shifter

An important feature of an integrated photonic device is its reconfigurability. This capability leads to two main advantages: error compensation due to fabrication tolerances and implementation of dynamic circuits so that we are able to change their functionalities during the experiment. A practical and relatively simple method widely employed for obtaining reconfigurable optical circuits is that of exploiting the thermo optics effect for inducing a



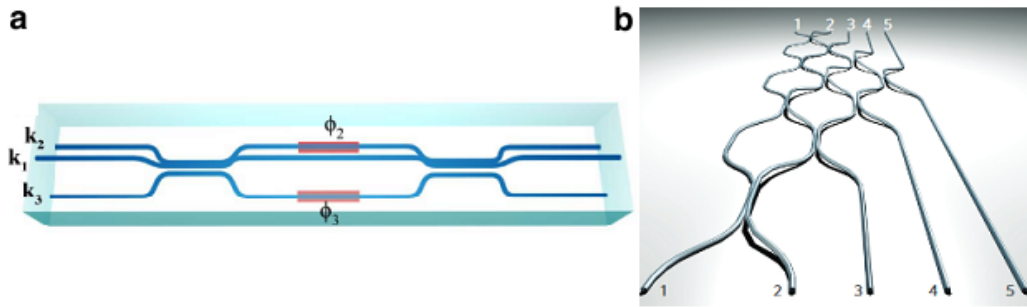


**Figure 2.4:** Schematic of a multiport interferometer. (a) 3D geometry of a 3-arm interferometer. Image taken from [23] (b) 5-arm interferometer. Image taken from [56]

localized refractive index tuning in several key points of the circuit. This operation is typically performed by means of resistive heaters placed in the proximity of the waveguides.

The fabrication of a reconfigurable device is possible with FLM, as demonstrate in [57]. In particular, it is made in three steps: first of all there is the normal waveguides writing inside the substrate. It follows the deposition of a gold layer of some nm by sputtering. Finally, the patterning of this metallic surface is made by cutting the gold, always thanks to a laser beam focused, this time, on the surface, in order to obtain the resistors which will act as thermo-optic phase shifter.

In particular in the work made by Flamini *et al* [57] was developed a tunable MZI. It was made in a aluminum-borosilicate glass, Eagle2000 by Corning, with pulses at 1030 nm with a repetition rate of 1 MHz, pulse energy of 330 nJ, an objective 50X (NA 0.6) and a translation speed of  $20\text{mms}^{-1}$ . The device had to work at telecom wavelength (1550 nm). The ablations on the gold instead were fabricated with 100 nJ energy pulses and a slow translation speed of  $1\text{mms}^{-1}$ . These ablations define the resistors which are written just above the arm of the interferometer where it has to be placed the phase shifter. The so inscribed rectangular resistors will dissipated energy as heat and, in Flamini's experiment, they were 0.3 mm wide (w), 20 mm long (L) and 50 nm thick (h). The value of the resistance is define by the second

Ohm's law:

$$R = \rho \frac{L}{h * w} \quad (2.8)$$

where  $\rho$  is, in this case, the gold resistivity.

The phase shift induced is due to the temporary local change in the refractive index which is proportional to the dissipated power  $P$  at the resistor  $R$  where  $P = \Delta V^2/R$ .

# Chapter 3

## Experimental Setup

In the first section it is described the setup employed for the fabrication of the integrated photonic devices.

In the second section it follows the explanation regarding setups and methods to characterize the photonic chips that have been produced.

## 3.1 Fabrication Setup

In fig.3.1 there is a sketch of the fabrication setup used to produce the optical devices presented in this thesis.

A cavity-dumped mode-locked oscillator generates femtosecond pulses at 1030 nm which pass through a system of dielectric mirrors to reach the machining area. At this point, thanks to a microscope objective, the writing beam is focused inside the underlying substrate. This last is stucked on a computer driven, three dimensional, linear motion system. Mounted on the translation stage there is a gimbal-based adjuster (GM100, Thorlabs) that, together with a set of mirrors, allows an accurate alignment for the setup.

A CCD camera is also used to collect the collimated back-reflected light from the sample surface. This is useful to set correctly the reference system for the writing process. Moreover, synchronized with the motion stage, it is present a mechanical shutter (SH05, Thorlabs) in order to block or not the laser pulses during the fabrication process and obtain the desired geometry.

The tuning of the average energy per pulse is made by the rotation of an half-wave plate placed before a to a Glenn-Thomson polarizer, at the beginning of the path.

In conclusion, two flip mirrors let to change the direction of the beam deviating it into a second harmonic generation stage and get, in this way, the half wavelength (515 nm) respect to the fundamental.

### 3.1.1 Laser source

The laser source is a cavity-dumped mode-locker oscillator [59] which was developed by the Max Planck Institut of Heidelberg (Germany) in collaboration with High-QLaser GmbH (Austria). The active medium is a KY(WO<sub>4</sub>)<sub>2</sub> crystal, doped at 5% concentration with Ytterbium. The wavelength emitted is 1030 nm. The pumping system is based on a InGaAs multiemitter laser diode bar at 980 nm and the optical pump power used is in the order of 15 W. The cavity is long 8.9 m and it is folded by a sequence of mirrors in a footprint of 90 cm x 50 cm.

The passive mode-locking regime, which generate a train of pulses at 17 MHz,

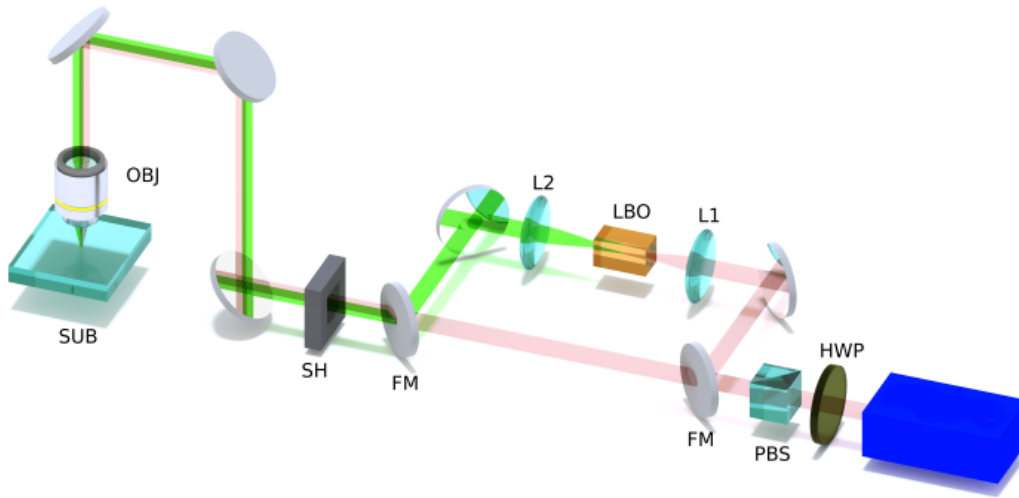


**Figure 3.1:** Schematic of the fabrication setup. A femtosecond laser beam at 1030 nm pass through an half-wave plate (HWP) and a Glenn-Thomson polarizer (PBS) which controls the the laser power intensity. A flip mirror (FM) can deviate the beam into a temperature controlled lithium triborate crystal (LBO) placed between to focal lens (L1, L2) with a 30 mm focus. This second harmonic generation stage generate a wavelength of 515 nm. It is then present a mechanical shutter (SH) synchronized with the motion system. The beam is finally focused inside the substrate (SUB), mounted on a 3D high-precision translation stage, through a microscope objective (OBJ). Image taken from [58]

is obtained by the utilization of SESAM (SEmiconductor Saturable Absorbing Mirror). A Pockels cell, combined with a thin film polarizer, performs the cavity dumping of the laser pulses. In particular on the Pockels cell acts an external electronic driver, synchronized to the train pulse, which can be tuned in its voltage and repetition rate. The thin film polarized needs instead to reflect, and so extract from the cavity, part of the pulse energy which is rotate in its polarization by the Pockels cell.

As already mentioned the pulse train is at 17 MHz and the repetition rate can be tuned, in the submultiples of 17 MHz, from few KHz up to 1.1 MHz. In conclusion, acting on the dumping ratio, is possible to get a pulse duration from about 250 fs to 400 fs according to the pseudo-solitonic regime sustained by the cavity [60].

### 3.1.2 Translation stage

The relative motion between the focal spot of the laser and the sample is ensured by a three-axis motion stage (Aerotech 3D FIBERGlide). An air-bearing, together with a brushless linear electric motor, permits to achieve an arbitrary 3D path in a volume of 100 x 150 x 5 mm<sup>3</sup> with high precision and smoothness.

Nanometric optical encoders monitor the stage position constantly leading to a control of the motion with errors below 100 nm. This system is computer controlled and is programmable by G-Code language.

## 3.2 Characterization Setup

In the following paragraphs will be briefly explained the characterization measurements and instrumentations adopted to test the device properties.

### 3.2.1 Optical microscope

The first check of the fabricated device is performed through an optical microscope.

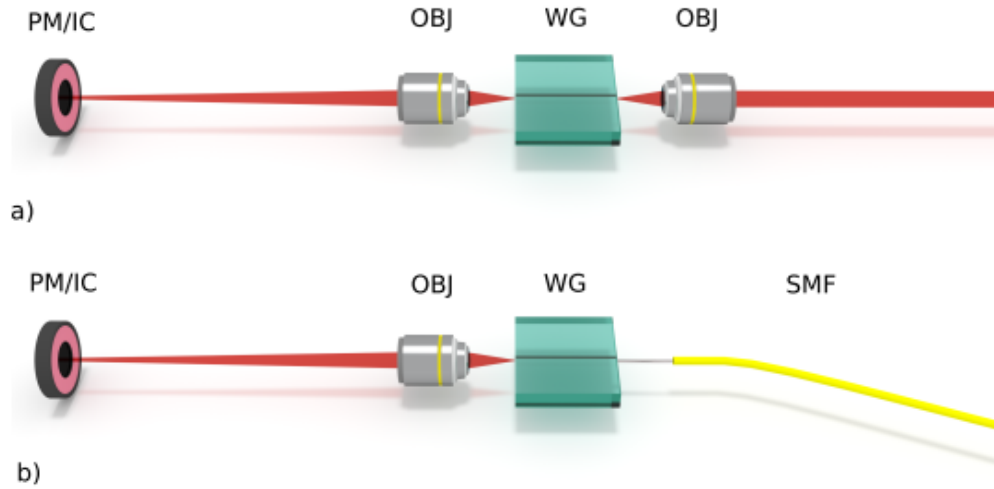


**Figure 3.2:** Schematic of the device coupling. (a) End-fire configuration. The laser beam is focused into the waveguide (WG) by a microscope objective (OBJ). Another objective is used in order to collect the light into a power meter head (PM) or an imaging camera (IC). (b) Fiber-butt configuration. Instead of an objective is used a single mode optical fiber (SMF). Image taken from [58]

By observing the surface of the substrate it is immediate to verify the presence of errors, such as interruptions or defects in the waveguide paths, and the uniformity of the writing process. It is also possible to look at the side of the sample analyzing the cross-section of the waveguides.

The optical microscope employed is a Nikon ME600 where is mounted an high resolution CCD Camera (PixeLINK B871) to acquire pictures with a computer.

### 3.2.2 Device coupling

A crucial step in the characterization of the waveguides is the measurement of the radiation confinement characteristics. In particular it can be done in two different ways.

The first method is shown in fig. 3.2a and it is the end-fire coupling configuration. It consists in focusing a coherent laser beam into the input facet of the waveguide through a microscope objective. In order to obtain a good

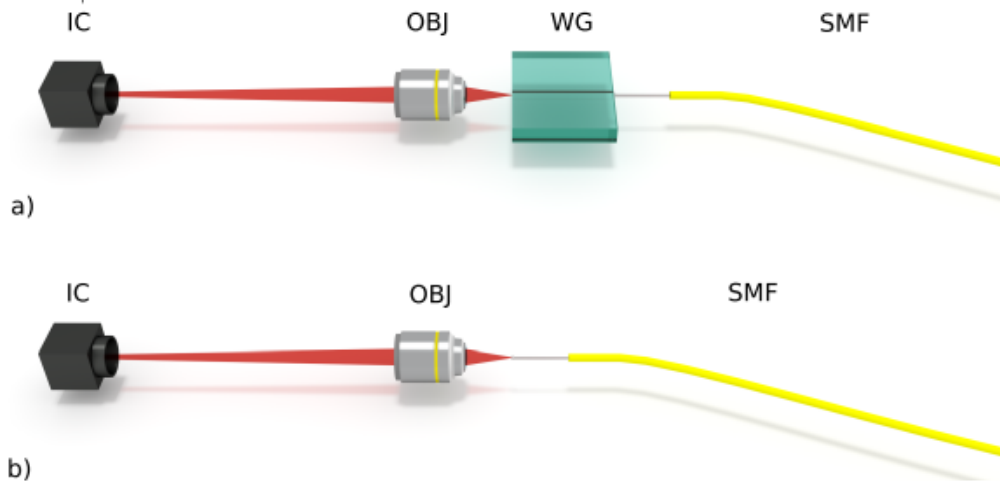


**Figure 3.3:** Schematic of the acquisition spatial intensity. (a) First step: collect the near field image of the waveguide (WG) by an imaging camera (IC). (b) Second step: for calibration is acquired the near field of the single mode fiber (SMF). Image taken from [58]

coupling efficiency the beam waist at the focal point has to match the mode radius, because of this the NA of the objective is consecutively chosen.

The other configuration (fig. 3.2b) is the fiber butt-coupling. In this case it is not used an objective but the light is directly injected by the fiber.

A precise and stable alignment of the objective (or fiber) is required since the waveguides mode is in the order of ten micrometer radius. Because of this, a three-axis micropositioner (NanoMAX, Melles Griot) with 50 nm resolution is employed to move the objective (or fiber). Moreover the sample is hold on a second stage, a four-axis manipulator (MBT 402, Thorlabs). In the latter, besides two linear translations, there are two tilting adjustments.

Finally, the collection of the output light is made with another microscope objective with higher NA mounted on a three-axis manipulator and the imaged on a power meter head or a video-camera.

### 3.2.3 Mode profile

A fundamental property that has to be understand is the spatial intensity profile  $I_{wg}(x,y)$ . A possible method for its measurement is by employing the



fiber butt-coupling configuration (fig. 3.3). The near field image of the output mode is imaged, by a microscope objective, onto a CCD camera, paying attention not to saturate its dynamic response. From this image it is possible to retrieve the mode intensity profile.

The same procedure is followed for the output of the fiber with a known mode diameter. This is necessary in order to calibrate the image dimension keeping the magnification ratio fixed so that the distance between the collection objective and the input of the camera remains unchanged.

The last step is to perform a numerical analysis on the acquired images. In particular, in case of single mode waveguides, the theory guarantees that the fundamental guided mode does not present any sign inversion and so the spatial field distribution is:

$$|E(x, y)| \propto \sqrt{I(x, y)} \quad (3.1)$$

The overlap integral of the guided and fiber mode profiles allows to calculate the coupling losses of the waveguides (eq. 3.5).

### 3.2.4 Losses measurement

The last important characterization regards the losses of the fabricated integrated circuit. It is crucial to quantify accurately the losses in quantum applications since they can heavily effect the performances. For instance in single photon measurement high losses will decrease the efficiency of the device because of an increase of the time of execution.

The Insertion Losses (IL) describe the attenuation of the optical signal because of the insertion of the sample and it can be expressed, in decibels, by:

$$IL_{dB} = -10 \cdot \log_{10} \left( \frac{P_{out}}{P_{in}} \right) \quad (3.2)$$

where  $P_{in}$  and  $P_{out}$  are the powers measured at the input and output, respectively.

The Insertion Losses can be decomposed in four different kind of terms: Fresnel Losses (FL), Propagation Losses (PL), Coupling Losses (CL) and Bending

Losses (BL). Each of them is due to a specific cause that will be explained in the next paragraphs.

**Fresnel Losses** are caused by the refractive index discontinuity at the air-substrate interface which brings to a partially reflection of the light. From the Fresnel equation for the reflection this kind of losses can be expressed as:

$$FL_{dB} = -10 \cdot \log_{10} \left( 1 - \frac{(n_2 - n_1)^2}{(n_2 + n_1)^2} \right) \quad (3.3)$$

where  $n_1$  and  $n_2$  are the two refractive indexes. In a common situation we have air ( $n_1 = 1$ ) and glass ( $n_2 = 1.5$ ) so that  $FL = 0.177$  dB for both interfaces, input and output.

**Coupling Losses** are related to the mismatch between the waveguide mode and the incoming light distribution. It can be represented by:

$$CL_{dB} = -10 \cdot \log_{10}(OI) \quad (3.4)$$

where OI is the overlap integral:

$$OI = \frac{|\iint E_{wg} E_{in} dx dy|^2}{\iint |E_{wg}|^2 dx dy \cdot \iint |E_{in}|^2 dx dy} \quad (3.5)$$

where  $E_{wg}$  and  $E_{in}$  are the field distributions of the waveguide and input fiber which can be numerically estimated as explained previously.

**Propagation Losses** are due to the rugosity and possible defects inside the waveguide. This contribution, unlucky, cannot be directly measured but only derived from others. In particular for a straight waveguide is:

$$PL_{dB/cm} = \frac{IL_{dB} - FL_{dB} - CL_{dB}}{l} \quad (3.6)$$

where  $l$  is the length of the waveguide.

**Bending Losses** are related to the distortion of a waveguide because of its possible not-straight geometry which deviate from the perfect translational symmetry.

In particular we look at the losses produced by a curved segment with radius  $R$ . As  $R$  increases the contribution decreases exponentially. To estimate these losses, several waveguides with different radii, but same bent path  $l_c$  are fabricated. The Bending Loss are then calculated as:

$$(BL_i)_{dB/cm} = \frac{(IL_i)_{dB} - (IL_{SWG})_{dB}}{l_c} \quad (3.7)$$

where  $(IL_i)$  are the Insertion Losses for the bent waveguide and  $(IL_{SWG})$  for the straight one.

In conclusion the overall Insertion Losses can be expressed by the equation:

$$IL_{dB} = CL_{dB} + 2FL_{dB} + BL_{dB/cm} \cdot l_c + PL_{dB/cm} \cdot l \quad (3.8)$$

where  $l$  is the total length of the waveguide and  $l_c$  the one of the curved section of the device.



## Chapter 4

# On Chip Quantum Estimation of Two Phases

In the first part of this Chapter it is presented the aim of this thesis and a general mathematical description of the device.

In the second part, it is discussed the design of the chip we developed. More details regarding the fabrication of the chip are going to be discussed in the next chapters.

## 4.1 Goal of the Experiment

The aim of this thesis is the fabrication of an integrated three-arm interferometer for the simultaneous estimation of two phases and the enhancement of this estimation outperforming the Standard Quantum Limit.

As already mentioned in the first Chapter, a multiparameter estimation is possible with multiport devices. Moreover it is possible to achieve a improvement in the accuracy of the measurement of the parameters employing quantum methods instead of classical ones.

In order to achieve all of this we will take advantage of the characteristics of FLM technique to develop an integrated three-arm interferometer stable and miniaturized. The interferometer is provided with reconfigurable phase shifters in order to dynamically tune the phase induced in the light injected in the device.

### 4.1.1 Mathematical description

A three-arm interferometer is made putting in sequence two balanced tritters. In Chapter 2 we described different ways to obtain a tritter, the one we use is the integrated version of the decomposition in couplers and a phase shifter, as it is shown in figure 4.1.

Always in reference to the figure 4.1, the first, theoretically loss-less, directional coupler is described by a field transfer matrix  $U_{T1}$ :

$$U_{T1} = \begin{pmatrix} \sqrt{R} & i\sqrt{T} & 0 \\ i\sqrt{T} & \sqrt{R} & 0 \\ 0 & 0 & 1 \end{pmatrix} \quad (4.1)$$

where  $i$  is the imaginary unit,  $R$  the reflectivity and  $T$  the transmissivity, already defined in Chapter 2 (eq. 2.6). The other two directional couplers ( $U_{T2}$  and  $U_{T3}$ ) are described by a similar matrix of equation 4.1, obtained by just sorting differently the rows and the columns, in order to take into account their operation on the specific optical modes.

Moreover it is also required an additional phase  $\varphi$  (fig.4.1) described by:

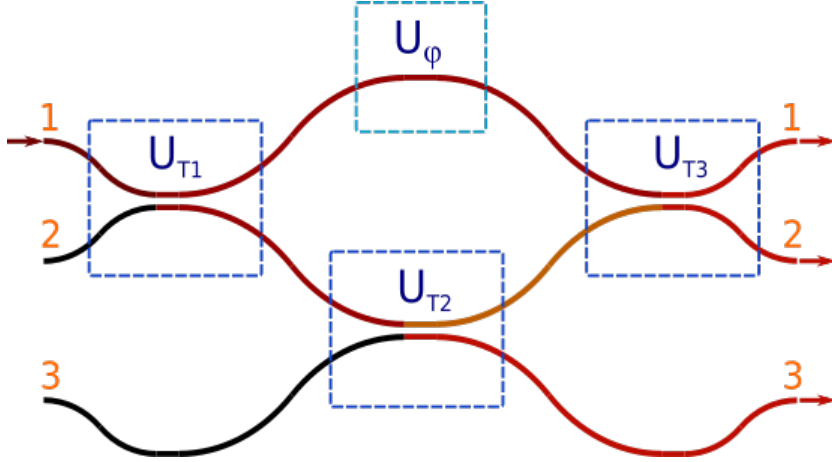


**Figure 4.1:** Design of a balanced tritter decoupled in three directional couplers and a phase shifter. Each of these elements are described by a unitary matrix.

$$U_\varphi = \begin{pmatrix} e^{i\varphi} & 0 & 0 \\ 0 & 1 & 0 \\ 0 & 0 & 1 \end{pmatrix} \quad (4.2)$$

The overall matrix of the tritter is calculated as  $U_{TRI} = U_{T3}U_{T2}U_\varphi U_{T1}$ .

In order to have a balanced tritter, so splitting the light from one input in three equal parts at the outputs, the first and third couplers need to have  $R = T = 1/2$ , while the second coupler has  $R = 1/3$  and  $T = 2/3$ . The phase  $\varphi$  has to be of  $90^\circ$ .

The final matrix  $U_{TRI}$ , which represent the whole tritter, is the already given eq. 2.7:

$$U_{TRI} = \frac{1}{\sqrt{3}} \begin{pmatrix} 1 & 1 & 1 \\ 1 & e^{i2/3\pi} & e^{i4/3\pi} \\ 1 & e^{i4/3\pi} & e^{i8/3\pi} \end{pmatrix} \quad (4.3)$$

**Tritter output probabilities** We now briefly analyze the output probabilities of a symmetric tritter in which is injected a three-photon Fock state  $|1, 1, 1\rangle$ , where each photon is in a different spatial mode.

Applying the tritter matrix  $U_{TRI}$  at the output we get  $-1/\sqrt{3}|1, 1, 1\rangle + \sqrt{2/3}(|3, 0, 0\rangle + |0, 3, 0\rangle + |0, 0, 3\rangle)$ . So we have all the possible configura-

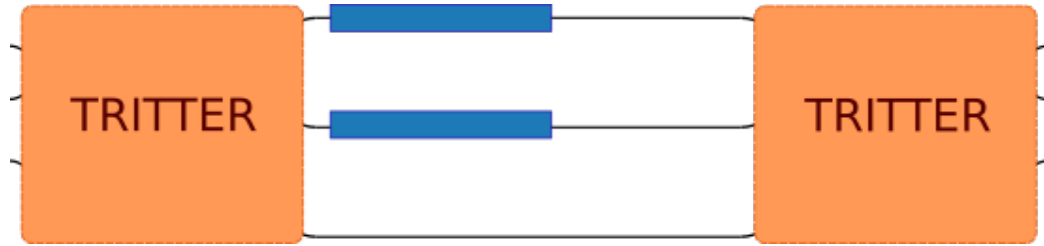


**Figure 4.2:** Basic design for the three-arm interferometer. There are two tritters in cascade to which set a inner phase of  $90^\circ$ . On the interferometer's arms at least two phase shifters, blue rectangles, are requested.

tions less the output with two photons in one port and the third in another, that because of the bosonic coalescence [52]. Only in case there is some delay that lets the input photons to be distinguishable this third kind of output can be detected.

### 4.1.2 Phase estimation

In order to have a three-arm interferometer two tritters have to be put in cascade. In addition, two phase shifters are required in order to tune the phases that we want to measure. In particular, these two phases have their value respect to a reference, which is the third arm looking at figure 4.3, but it can be arbitrary chosen. The overall device is so described by  $U_{INTERF} = U_{TRI}U_\theta U_{TRI}$ , where  $U_\theta$  is the matrix describing the phase shifts. With a different tuning of these phases a different fringe pattern can be detected.

In particular, by injecting in it a Fock state, we expect to see interference fringes characterized by non-classical visibility. Thanks to this quantum approach we can increase the value of the Fisher information extracted by a measurement and, especially, achieve a simultaneous estimation of two phases as it is theoretically discussed in the work of Spagnolo *et al* [23]. The three output probability distributions show an interference pattern as a sum of different harmonics up to  $\cos(3\theta)$ , as we expected by the discussion in the first Chapter (1.1.3).

In addition to this super-resolution feature, always as already mention in the



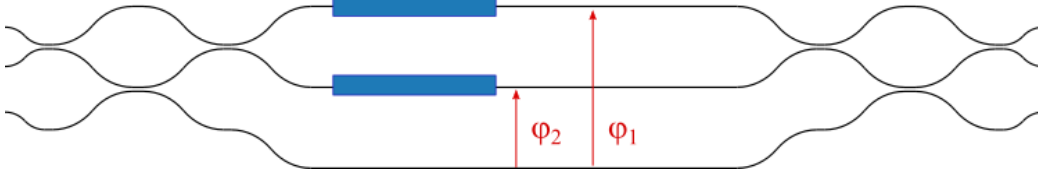


**Figure 4.3:** *Three-arm interferometer. Along the arms are inserted the phase shifters in order to tune, respect to a reference (the third arm in this case) the phases to measure.*

first Chapter (1.2.5), the employment of quantum techniques lead also to the enhancement in the phase estimation. In particular the overcoming of the Standard Quantum Limit (SQL) scaling of  $\sqrt{N}$  in the precision of the measurement, where  $N$  is the number of photons used.

## 4.2 Design of the chip

In order to have a three-arm interferometer we have already explained in the previous paragraphs the need of two tritters, with their phase shifter, and, at least, two other phase shifters on two different arms of the interferometer (fig.4.3).

We will adopt thermo-optics phase shifter to do this work. Thus, thanks to the heat dissipation coming from the electrical current flowing through these resistors, as explained in Chapter 2, we can variate the phase induced in the light passing in the underlying waveguides. More details regarding interferometer's resistors placing, geometry and functions will be discussed in Chapter 6.

There are, then, two ways to develop the overall device. It can be made in just one chip or divided in two, in both cases there are advantages and disadvantages. In particular have more chips have drawbacks regarding their alignment and high losses. On the other hand, it is easier to characterize a single tritter per time, also because a full study of all the parameters of the complete interferometer is not possible. In particular retrieve all the splitting ratios of both tritters in sequence cannot be accomplished when they are in the same chip. Anyway, through some simulations, it has been

studied situations with slightly different splitting ratio values and they can be tolerate without problems. For these reasons we decided to opt for a unique device.

In conclusion, in order to perform the best possible characterization of the device, an algorithm as been develop. It will be explained in Chapter 6.

# Chapter 5

## Tritter

In this chapter it is explained in detail the experimental optimization of the tritter, the basic element for the three-arm interferometer.

In the first part it is described the process to decide the fabrication parameters for fabricating a low loss and single mode optical waveguide at the desired wavelength.

Then it is discussed how we fabricated the tritter and, in particular, the reasons for the choice made about the implementation of an active control of the phase instead of a passive one.

## 5.1 Optimization of the fabrication parameters

### 5.1.1 Choice for the fabrication parameters

As discussed in Chapter 2 there are many parameters from which FLM technique depends.

Our device, fabricated in aluminum-borosilicate glass (EagleXG, Corning Inc.), has to work at 780 nm since it is the wavelength required for the final experiment. In order to find the optimum parameters for this wavelength, many straight waveguides were fabricated with different parameters and then characterized. In particular, we explored a fabrication window by varying both the average fabrication power (ranging from 170 mW to 280 mW by steps of 10 mW) and the sample translation speed (using the values of 20, 30 and 40 mm/s). The final choice for these two parameters was done by using the combination which produced the waveguide with lower propagation loss (0.9 dB/cm).

The choice of the other relevant fabrication parameters (namely the repetition rate and the focusing NA) was based on the literature and the experience gained from previous experiments. In table 5.1, all the fabrication parameters are listed. We also decided to fabricate our optical circuit at the depth of 30  $\mu\text{m}$  beneath the sample top surface. Indeed deeper is the waveguide higher has to be the power dissipated on the resistive heater with the aim of tuning the phase of the light. An excessive power dissipation could lead to an overall temperature increase and a possible damage of the chip. Anyway the fabricated waveguides cannot be too superficial since the sensibility to surface roughness and defects could increase the propagation losses.

In the characterization for the choice of the parameters we have also numerically calculated the size of the mode. In particular its diameter, when the amplitude is  $1/e^2$ , is, in the two axis directions,  $X=7.49 \mu\text{m}$ ,  $Y=8.28 \mu\text{m}$  with the light horizontally polarized, and  $X=7.16 \mu\text{m}$  and  $Y=8.39 \mu\text{m}$  with the light vertically polarized.

Fabrication parameters	
Material	borosilicate glass
Wavelength	1030 nm
Repetition rate	1 MHz
Pulse power	250 mW
Translation speed	30 mm/s
Objective	50X, 0.6 NA

**Table 5.1:** Waveguide writing parameters used for realizing devices for 780 nm.

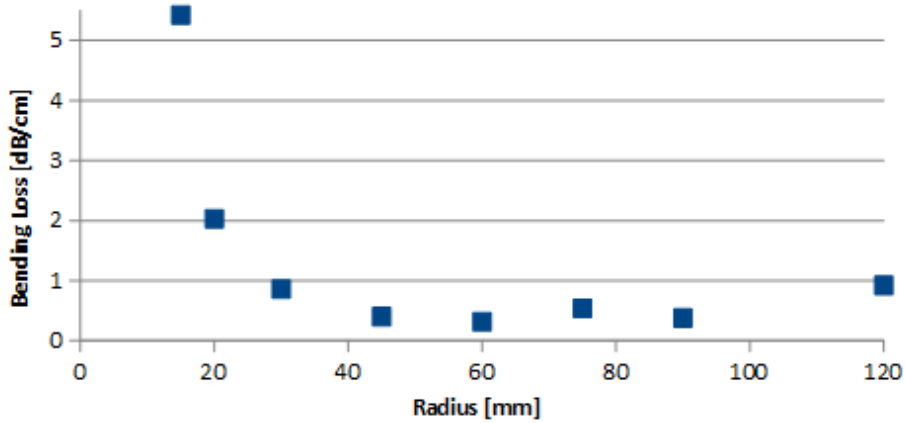


**Figure 5.1:** Bending losses for waveguides written with the parameters of table 5.1.

### 5.1.2 Bending losses

Subsequently at the choice of the fabrication parameters we fabricated with these a series of curved waveguides with different radii. We characterized them, as explained in paragraph 3.2.4, in order to measure the bending losses. Thus we measured the insertion losses of the bended waveguides, taking  $l_c = 25$  mm (eq. 3.6). The results are shown in fig.5.1. From them we can conclude that it is possible to employ a radius of 60 mm. In this way we still have low losses even using a short radius and, so, with the possibility of fabricate shorter devices thanks to tight curves.

## 5.2 Tritter parameters

### 5.2.1 Coupling lengths

Before the fabrication of the tritter we have proceeded with the fabrication of several directional couplers. In this way we could choose the coupling coefficient  $k$  in order to get the desired reflectivity and transmissivity. The mathematical description of a tritter, and so the reason why we need this specific setting, was already given in Chapter 4. An explanation of the coupling coefficient and the relative properties to which it is connected was given in paragraph 2.3.1.

Thus we fabricated four sets of couplers, with distances between 9 nm and 12 nm, each set is constituted by 11 couplers with increasing coupling length (fig.5.2). Fitting the data acquired the values  $k$  and  $\phi_0$  of the reflectivity function  $R = \sin^2(kL + \phi_0)$  were extrapolated. It is to be noticed that, respect to the equation given in paragraph 2.3.1, it is present also the phase term  $\phi_0$ . The reason is why the coupling of the light starts a bit before the actual coupling region, with the approaching of the waveguides. Analyzing these data we finally choose to work with a distance of  $d=9 \mu m$ , it gives a shorter coupling length and, so, an overall shorter device. The fitted parameter's values are  $k = 0.407 \text{ mm}^{-1}$  and  $\phi_0 = 0.429 \text{ rad}$ .

With the fitted parameters we got it is now possible to calculate the coupling lengths we want just solving the equations:

$$\begin{cases} R1 = \sin^2(kL_1 + \phi_0) = \frac{1}{2} \\ R2 = \sin^2(kL_2 + \phi_0) = \frac{1}{3} \end{cases} \quad (5.1)$$

To conclude, now we have the coupling lengths  $L_1$  and  $L_2$  related to the desired reflectivity for the couplers which compose our balanced tritter.

### 5.2.2 Phase

As explained in the previous Chapter another requirement in order to have a balanced tritter is a phase of  $90^\circ$  (fig. 4.1). It can be achieved in different

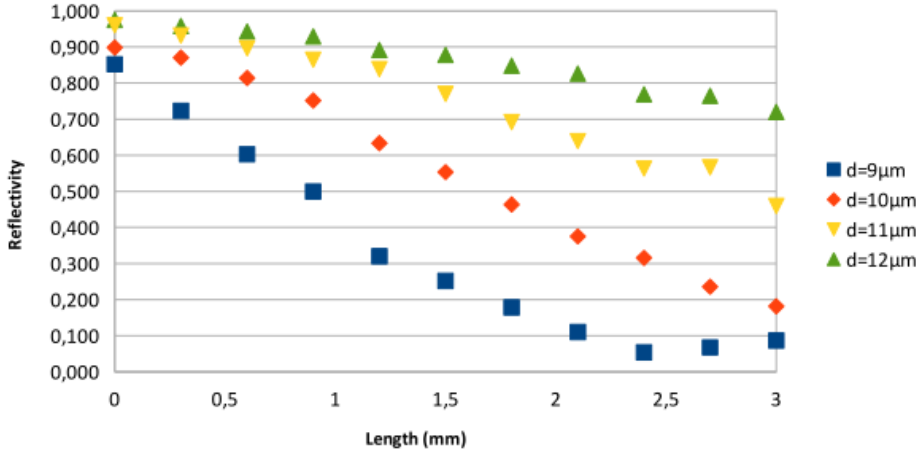


**Figure 5.2:** Data of four sets of directional couplers. The one we chose to fit is  $d = 9\mu\text{m}$  from which we get  $k = 0.407\text{mm}^{-1}$  and  $\phi_0 = 0.429\text{rad}$ .

ways: passive or active.

A passive phase is implemented doing a distortion of the optical path. An active phase, instead, is dynamically controllable tuning a thermo-optic phase shifter placed above the waveguide. This active implementation requires a longer preparation, since it is necessary to write the ablation after sputtered the gold, and a more complicated setup for the characterization. It is more time-expending and the possibility to make errors increases. Thus we firstly decided to try with the passive phase implementation.

**Passive phase** The passive phase implementation is made extending the path of the first arm changing the value of the angle  $\alpha_3$ , as showed in figure 5.3. The difference in the optical path  $\Delta C$  is related to the desired phase  $\Delta\Phi$  through the equation:

$$\Delta C = \frac{\lambda}{2\pi n} \Delta\Phi \quad (5.2)$$

where  $n$  is the refractive index of the guided mode. Then, in order to have the connection between  $\Delta C$ , and so  $\Delta\Phi$ , and the value of the angle  $\alpha_3$ , the

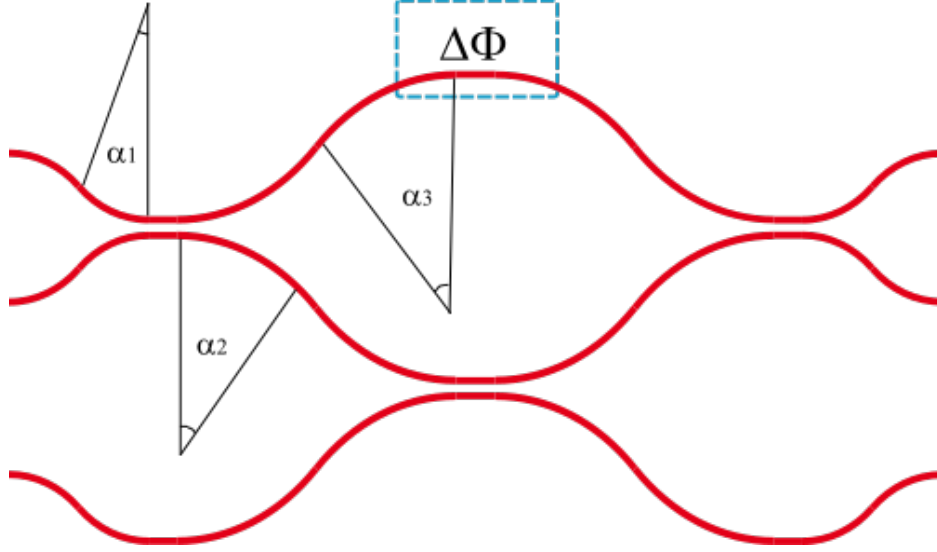


**Figure 5.3:** *Tritter geometry, the angles  $\alpha$  represent half-Sband angle.  $\alpha_3$  is related to the passive phase implemented in order to have a longer optical path.*

equation to be solved is:

$$\alpha_3 - \sin(\alpha_3) = \frac{\Delta C}{4R} + \alpha_2 - \sin(\alpha_2) \quad (5.3)$$

where  $R$  is the radius of the S-bands and  $\alpha_2$  is the angle indicated in fig.5.3. This is an equation of Kepler's kind ( $x - E \sin x = M$ ) and cannot be solved analytically, unless we use as approximation  $\sin(x) \sim x$ , valid in our case, since the angle  $\alpha_3$  is small enough, around  $2^\circ$ . Some numerical examples of the relation between phase difference, optical path difference and angle are shown in table 5.2.

A group of tritters with several passive phases was so fabricated, using the value of  $k$  found previously. The chip was then characterized injecting light in one input and looking for a good splitting of  $1/3$  at each output.

In figure 5.4 is shown an example of the data we get. In particular we compare the data acquired with the simulations, finding a good agreement with these. It is clear how output 3 is always independent by the phase and all outputs are also not influenced by it when the light enters from input 3. We also notice that the phase where the intersection of the three lines



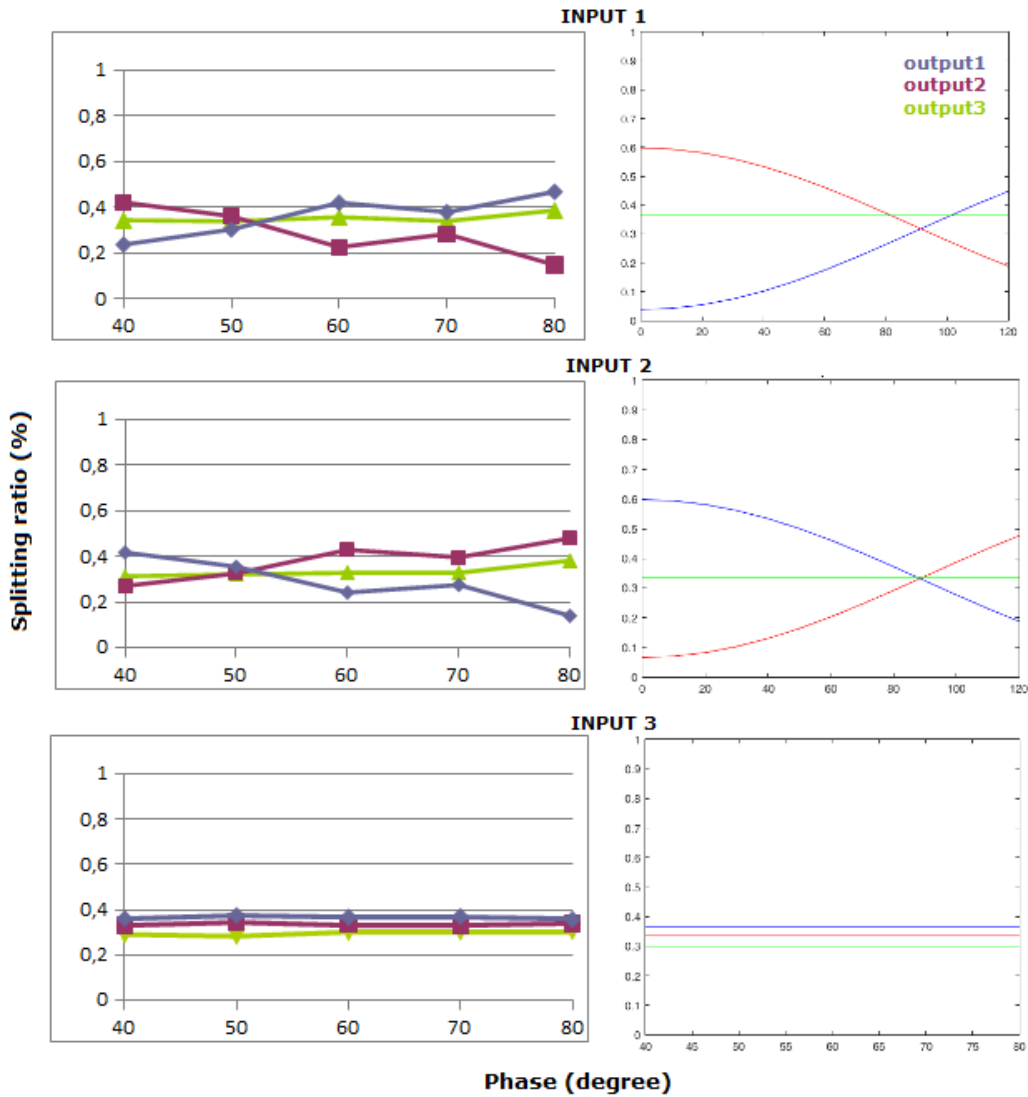


**Figure 5.4:** Example of comparison experiment/theory for  $k=0.40 \text{ mm}^{-1}$ . On the left the experimental data on the right the corresponding simulation (using the measured splitting ratio). From top to bottom: light inject in input 1, input 2 and input 3. The different colors correspond to the different output as reported in the legend at top right. The intersection of the three lines takes place at different phase, even for the same input, because of the unknown intrinsic phase of the interferometer.

$\Delta\Phi$ [°]	$\Delta C$ [nm]	$\alpha_3$ [°]
40	60	2.59
90	130	2.65
120	170	2.69
180	260	2.76

**Table 5.2:** Values for the phase difference, relative optical path difference and relative angle.

takes place is different respect to the simulation. The reason is related to the existence of an unknown additive phase. This phase is due to the coupling between the second and third waveguides, as explained in [61].

We conclude that we get good splitting ratios, but a not so good reproducibility of the passive phase implemented since it is not fully controllable from one fabrication to the other. This is the reason why we decided to try to implement an active control of the tritter phase.

**Active phase** Use an active phase means to build a thermally reconfigurable device. This can be done employing thermal optical shifters such as the ones discussed in Chapter 2. Thus, in the fabrication of the waveguides all the paths of the three arms are equal. Then a thin layer, tens of nanometers, of gold is sputtered on the glass top surface. On this gold layer, always with a laser, some ablations are made in order to build the wanted resistor. In the resistor we will let the current flow and, so, it will dissipate heat that will influence the underlying waveguide, changing the phase according to the power dissipated. In order to optimized the positioning of these heaters has to be taken in account the geometry of the device, especially the reciprocal locations of the waveguides. More details regarding this procedure, and the correlation with the induced phase shift, will be discussed in Chapter 6.

In figure 5.5 is shown the design of the active tritter. The resistor is made in curved fashion, partially following the S-band. The decision of build a curved heater is made in order to increases the efficiency of the thermo-optic phase-shifter on the underlying waveguide, following its profile. The resistor is 5.3 mm long, 0.1 mm wide and 60 nm thick. The measured resistance

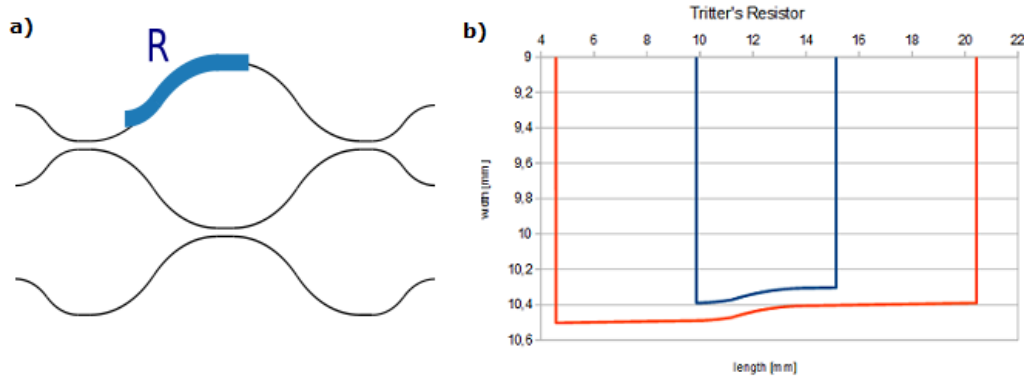


**Figure 5.5:** Active tritter design. a)  $R$  is the resistor written on half  $S$ -band and a straight guide. b) Zoom on the resistor's cuts (blue and red) designed.

value is  $100 \Omega$ .

Also in this case we characterized the tritter injecting the light in one input looking at the three outputs. The result we get is in figure 5.6. We can recognize the same feature we have in the simulations, like in the passive phase implementation, where output 3 is always constant and the other two change as a sine function. We can also see we get two points of intersection which correspond to  $90^\circ$  and  $270^\circ$ . Moreover these intersections come when the splitting ratio is around 33%, as expected. Because of these very good results and the possibility to easily tune the device in different states, we decided to opt for an active implementation.

The picture 5.7 shows the real device mounted on the stage between the two objectives. The connectors, the two at the borders, let the current flows from one to the other, through the resistor. In order to protect the chip some UV glue was put on it.

To conclude, a successful dynamic tritter working at 780 nm has been fabricated. Its structure and geometry is the one made with directional couplers following the integrated version of a multiport beam splitter decomposition. In last chapter it is discussed how, putting two of these tritters in cascade, it has been fabricated a three-arm interferometer.

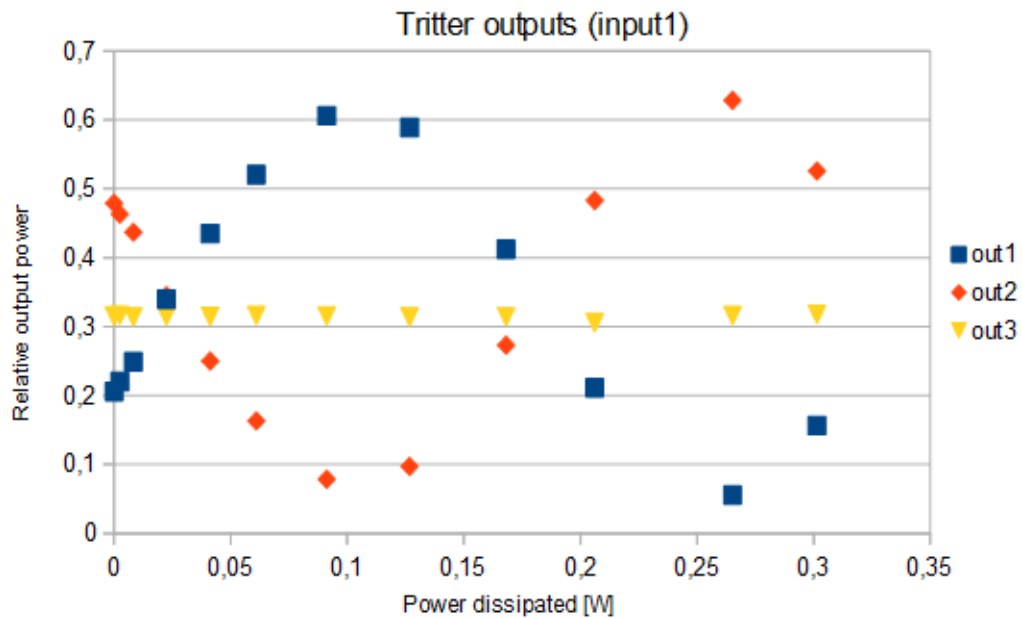


**Figure 5.6:** Three outputs of the dynamic tritter entering from input1. There are 2 points where all the three lines cross and where it is achieved a splitting of 33%.

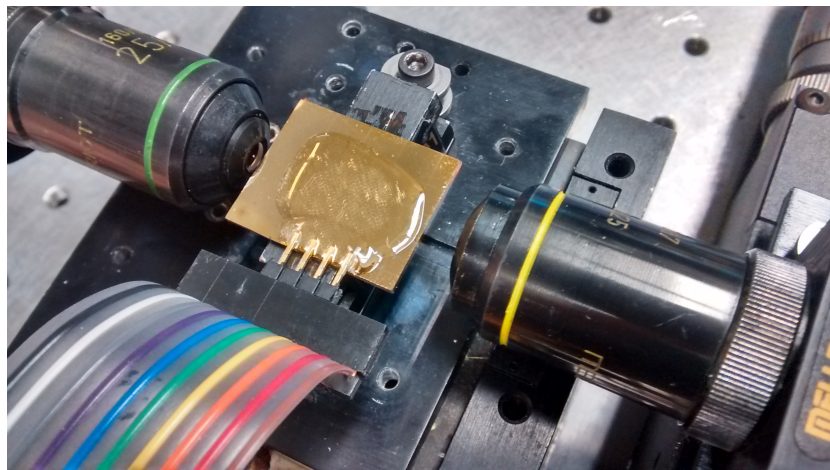


**Figure 5.7:** Photo of the tritter put between the two objectives, launch (10X) and collection (25X). It is covered by UV glue for protection, the current flows between the two connectors at the sides while the two in the middle are disconnected and put just to increase the robustness.

# Chapter 6

## Three-arm interferometer

In this chapter we will first discuss about the interferometer fabrication, especially regarding its tunable phase shifters. We will focus on the technical method of connectorization of the electrodes and, then, the characterization method of the whole interferometer.

Finally the experimental data are analyzed and discussed.

## 6.1 Interferometer design

As already said, a three-arm interferometer is built putting in cascade two balanced tritters. The final layout of this device is depicted in figure 6.1a. The input and output ports of the device are equally spaced by a distance of  $127 \mu m$  which allows to eventually couple in and collect the optical signal from the device by means of a standard fiber arrays. All the curved segments have been fabricated with a bending radius of  $60 m$  and we used the optimized geometry of the tritters described in the previous chapter, adopting the reconfigurable configuration. The central region of the interferometer is composed by three straight optical paths which are  $20 mm$  long, for allowing the fabrication of the thermal phase shifters for driving the interferometric experiments. These optical modes are separated by  $245 \mu m$ . The whole device have been designed in such a way that all possible optical paths, which connect any input to any output, are of the same length, for avoiding problems related to the finite coherence length of the probe light used. The total length of the interferometer realized is approximately  $75 mm$ .

Regarding the phase-shifters along the interferometer's arms there are six of them, two per arm: R1, R2, R3, R4, R5, R6 (fig. 6.1b). Note that the minimum number of phase shifters, required to get full control of the interferometric fringes at the device output, would have been of only two, placed on two different arms, since there are only two independent phases in a three mode interferometer. Additionally, a third one is required in order to have a tunable reference. All the others are not strictly necessary, but they can be useful as backup or to increase the flexibility and possible experiments that can be performed. It is important to stress that this increase in the number of resistors does not complicate significantly the overall device design. The length, and so the losses, of the arm gets longer just putting the fourth phase-shifter and, since the optical path of each arm has to be the same, we have already gained space to insert also the last two shifters without any further modification of the waveguides inscribed inside the glass. Thus the only possible drawback in increasing the number of phase shifters is represented by a more complex (but doable) design of the electrical circuit for the

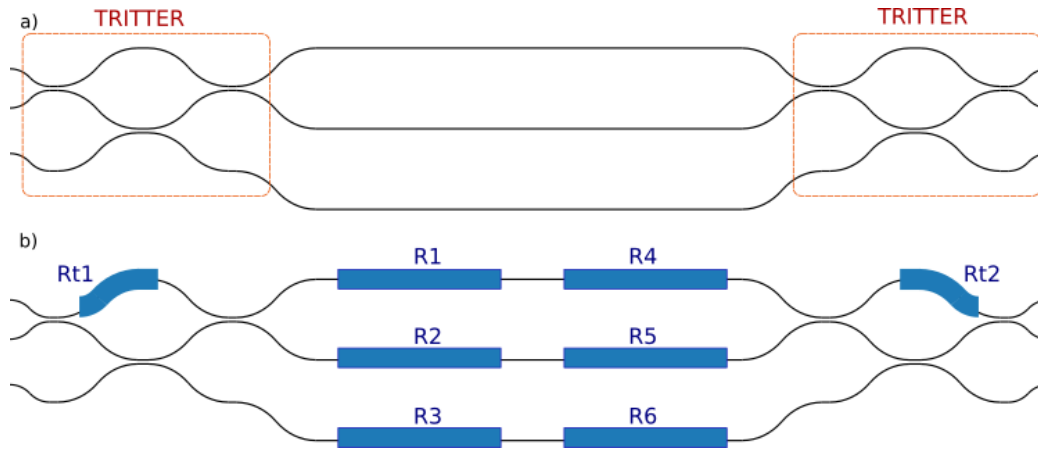


**Figure 6.1:** *Design of a three-arm interferometer. (a) Waveguides: two integrated planar tritter in cascade divided by the arms of the interferometer. Input and output ports put at distance of  $127\mu\text{m}$ . (b) In evidence the position of the resistors (thermo phase shifter) written above the waveguides, on the sputtered gold surface.*

resistor driving.

In order to compensate for an intrinsic variability of the fabrication process (and consequently, of the coupler coupling coefficient) we fabricated several interferometers within the same chip, each of it with finely tuned geometrical parameters. A set of single directional couplers fabricated contextually to the interferometers helped in understating which of it showed the best performances in terms of couplers splitting ratios.

The overall insertion losses of the final device, measured by in-coupling the light with a optical fiber and collecting it with a microscope objective, result around 7.5 dB.

Once we did that, and after checking with the microscope there are no interruptions in the waveguides paths of the chosen interferometer, it was possible to go on with the operations to make the device dynamically tunable.

### 6.1.1 Thermo-optic phase shifters

In Chapter 2 was already discussed the temperature-induced refractive index variation, and so the consequent phase shift, due to the dissipated power

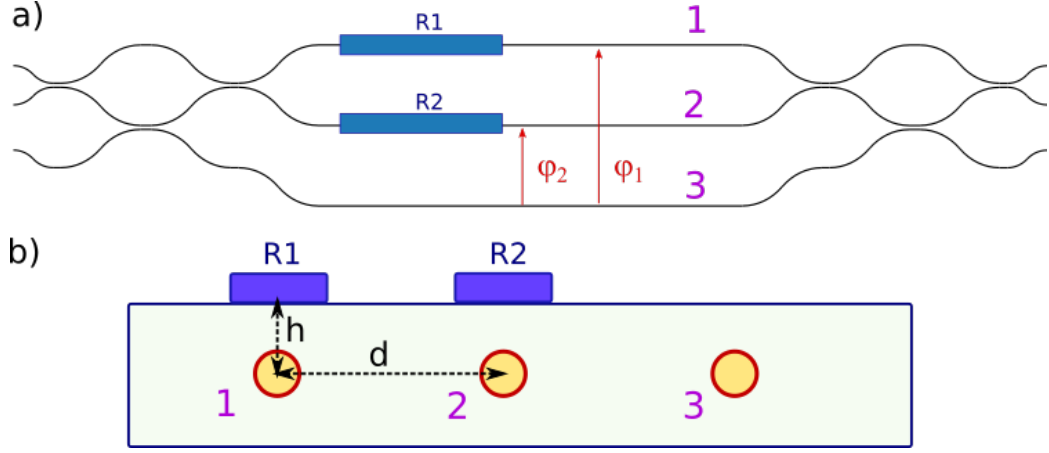


**Figure 6.2:** a) Design of the interferometer assuming the third arm as the origin, the two phases  $\varphi$  as indicated related to the two resistors R1 and R2. b) Side view of the chip,  $h=30\mu\text{m}$ ,  $d=245\mu\text{m}$ .

( $P_{diss}$ ) as heat. In particular the proportion between these two parameters is given by the equation:

$$\varphi = \alpha P_{diss} \quad (6.1)$$

where  $\varphi$  is the phase shift induced. The proportionality coefficient  $\alpha$  depends on the geometric, thermal and optical properties of the material, in our case the glass EagleXG. In particular, assuming a wire-like resistor, and neglecting power dissipation from the top surface (since air is an insulator) the temperature inside the substrate decays following a logarithmic function. From these approximations, an analytic equation for  $\alpha$  can be calculated [57]:

$$\alpha = \frac{2n_T}{\lambda} \frac{1}{k} \ln \frac{\rho_1}{\rho_2} \quad (6.2)$$

where  $n_T$  is the thermo-optic coefficient ( $1 \cdot 10^{-5} K^{-1}$ ),  $k$  is the thermal conductivity ( $0.9 Wm^{-1}K^{-1}$ ),  $\lambda$  is the wavelength ( $780 nm$ ) and  $\rho_1$ ,  $\rho_2$  are the distances between the interferometer arms and the resistor.

Assuming the configuration of fig.6.2a the two phases are correlated with



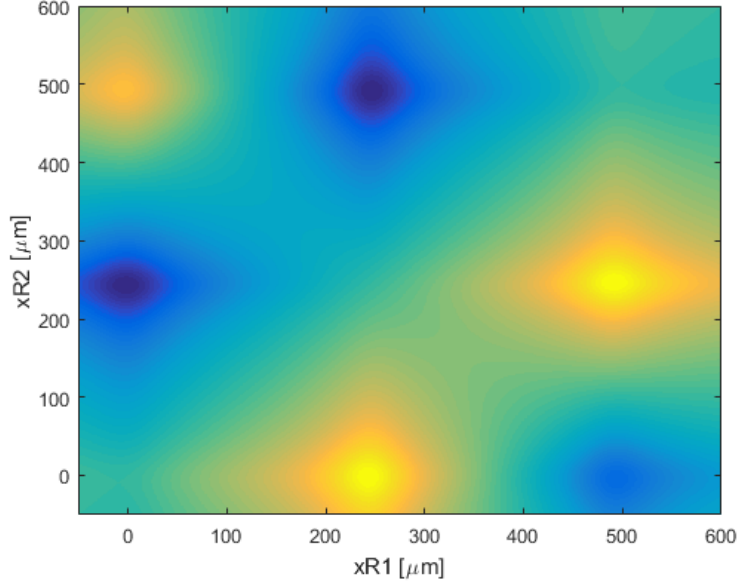


**Figure 6.3:** Result of the simulation where the color indicates the value of the determinant of the  $\alpha$  matrix and where the positions of the resistors  $R1$  and  $R2$  are varied. The colormap used for this plot is Matlab's Parula. The yellow points correspond to the graph maxima, while the dark blue one correspond to the local minima.

the power variation in this way:

$$\begin{pmatrix} \varphi_1 \\ \varphi_2 \end{pmatrix} = \begin{pmatrix} \alpha_{11} & \alpha_{12} \\ \alpha_{21} & \alpha_{22} \end{pmatrix} \begin{pmatrix} P_1 \\ P_2 \end{pmatrix} \quad (6.3)$$

The off-diagonal terms are the unavoidable cross-talks caused by the proximity of the resistors to different waveguides. It is actually convenient to minimize these terms, thus maximize the diagonal ones in order to keep the dependence of each phase correlated with just the power dissipated on its resistor.

In order to decide the best geometry, and so find the optimum position for the resistors respect the waveguides, we performed a simulation. As expressed in eq.6.2  $\alpha_{ij} \propto \ln \frac{\rho_{ij}}{\rho_{3j}}$  where  $i$  is the index of the waveguide and  $j$  the one of the resistor (fig.6.2b). For instance, keeping the third arm as the origin,  $\rho_{22} = \sqrt{h^2 + (xR2 - d)^2}$  where  $xR2$  is the independent variable

which has to be optimized. Since, as mentioned above, we want to avoid the crosstalk the parameter that we want to maximize is the determinant of the  $\alpha$ -matrix of eq.6.3.

The result of the simulation (fig.6.3) leads us, as it is intuitive, to put the heaters just above the waveguides. In particular, we can notice two points of maximization, one corresponding to the geometry of fig.6.2a, the other putting R1 on the second waveguide and R2 on the third, so just a shift. There is also another local maximum putting the heaters on the waveguides one and three. The points of minimum are just the symmetric positions of the resistors and, so, a change in the sign of the determinant.

Finally, after the deposition of a layer of gold on the glass, we performed the cuts on it, obtaining the wanted geometry (fig.6.4). The parameters we used to perform these ablations with the wavelength of 515 nm are: a power of 100 mW and a translation speed of 2 mm/s. Moreover, to achieve a better cutting, we pass on the same ablation 8 times. Each resistor has its electrode and there is a unique mass for all of them. The tritters resistors are the same of fabricated with the same geometry described in Chapter 5.

The straight resistors of the interferometers are 7 mm long, 0.1 mm wide and 55 nm high. The experimental resistances measured are in agreement with our design, besides the tritters resistances which have a higher value instead of lower, that was what we expected because they are shorter. The reason of this difference is probably due to the not-homogeneous gold deposition. The tritters are, indeed, closer to the edge of the chip that is quite long (75 mm) and it is clear just looking at the sample that at the extremes less gold has been deposited. Because of this thinner layer, probably 20 nm less, the value of the resistances are grown.

## 6.2 Connectorization method

Once that the resistors have been defined on the gold, it is necessary to connect the electrodes to their wires and, so, to the power supply. In order to improve the common method our group used until now, consisting in copper wire to be attached manually to the substrate, another one, more

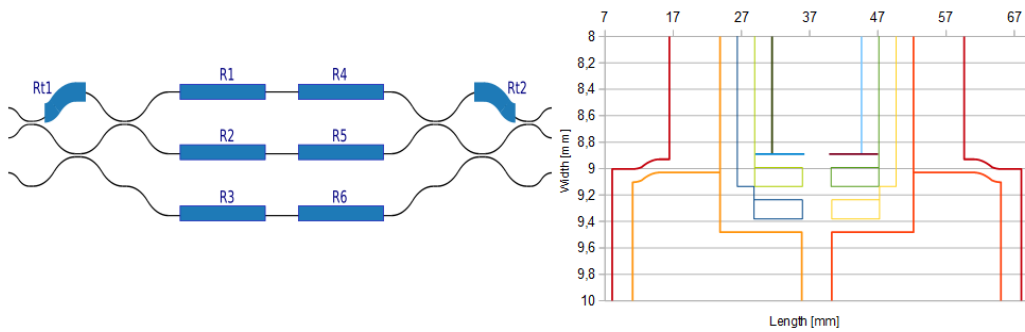


**Figure 6.4:** On the left the design of the interferometer. On the right the structure of the cuts in order to obtain the design. Each color correspond to a different cut. There is a common mass connecting all the resistors on the interferometer's arms and the tritter's resistors (which is not possible to see due to the zoom).

elegant and robust has been developed.

First of all, instead of using copper wires, a set of different commercial kinds of pins has been taken in consideration. After some trials we select the most convenient pin-structure for our purpose. The pins have to be attached easily at the side of the substrate and to be connected and disconnected to the wires without applying a too high force. Each pin is at a fixed distance of 2.54 mm from the next one.

The gluing on the gold surface is made through a thermo-conductive glue which takes about 2 days to completely dry and, so, guaranteeing a good endurance. In order to put the pin in the correct position it is possible to employ a micromanipulator so that a very good positioning can be achieved (fig.6.5).

Once the resistors values are checked and we are sure that our device can work properly, it is better to protect it from possible damages since the gold surface is quite delicate and easy to scratch. Again, for accomplishing this step we tried two methods: we tried to covered the electrical circuit alternatively with UV glue or by a new one, employing polyvinyl acetate (PVA) which is safer to use.

First of all we tried if, with PVA, there was a change in the value of the resistances and if it can guarantee a good mechanical endurance connecting

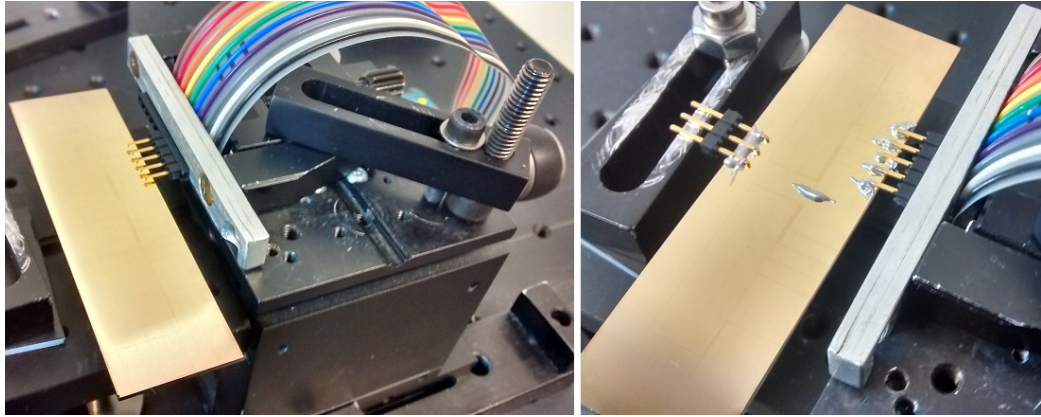


**Figure 6.5:** *Pictures of the new connectorization method. Thanks to a translator is possible to precisely position the pins and take them still until the dry off of the glue.*

and disconnecting the connectors. Both trials had a positive result, even if it is necessary to wait a couple of days in order to let the PVA dry completely. Then we tried to let the current to flow and dissipate some power from the resistors. By increasing the dissipated power we could see that, when it was approaching 1 W, the PVA started to melt. That because the PVA fusion temperature is around  $80^{\circ}\text{C}$ , which is lower respect the one of UV glue. For this reason, and because of longer drying time, we decided to go on with the UV glue method.

### 6.3 Characterization method

The three-arm interferometer has to be set in a known configuration and the values of  $\alpha$  coefficients measured. In order to do that an algorithm has been developed, through a simulation supported by analytical calculus. This method can be divided in three parts.

**Interferometer phase setting** Two resistors on the interferometer's arms need to be connected in order to let the current flows through them and, so, modify the phase of the light passing in the waveguides. In particular, at this stage, we inject the light in input 3 and collect it from output 3 (fig.6.6).

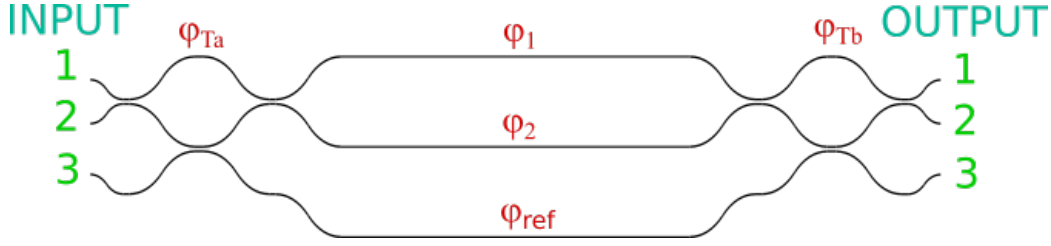


**Figure 6.6:** In the picture are showed all the parameters we can set in order to characterized the interferometer.

This is necessary since in this way we are independent with respect to both tritters phases, as shown in fig.5.4 where the the third output is constant. In that case we were talking about a tritter, so entering from every input the third one is independent, now, since we have two tritters in sequence, we have this situation just entering from the third input.

Now, tuning the voltages of the two resistors accurately, we have to reach a minimum in the light power detected. Once we reached that minimum it means we have set the phases difference ( $|\varphi_1 - \varphi_2|$  and  $|\varphi_2 - \varphi_{ref}|$ ) at  $60^\circ$ , as now we proof the overall matrix of the interferometer is  $U_{INT} = U_{TRI}U_\theta U_{TRI}$  and, so,  $E_{OUT} = U_{INT}E_{IN}$ . Since we are interested only in input 3 and output 3 we select this result ( $E(3)_{OUT}$  with  $E_{IN} = [001]^T$ ), remembering that the intensity is  $I = |E_{out}|^2$ . Assuming  $\varphi_2 = 0^\circ$  what we have is:

$$I(3 \rightarrow 3) = 1/9[3 - 2(\cos\varphi_1 + \cos\varphi_{ref}) + 2\cos(\varphi_{ref} - \varphi_1)] = 0 \quad (6.4)$$

that we put equal to 0 since we want to minimize it. The solutions to this equation are  $\varphi_1 = \pm 60^\circ$  and  $\varphi_{ref} = \mp 60^\circ$ .

**Tritter B setting** Again, entering from input 3, thus avoiding influences from the first tritter phase (A), we move either on output 1 or 2. In this way we can set the phase of the second tritter (B). Also in this stage what we are looking for is a minimization of the light power at the output which is correlated to a phase setting of  $90^\circ$  or  $-90^\circ$ , which is still a good working point for the functioning of tritter b.

Also in this case we can analytically prove this result starting with the phases

$\varphi_1 = 60^\circ$ ,  $\varphi_2 = 0^\circ$ ,  $\varphi_{ref} = -60^\circ$  and with  $E_{IN} = [001]^T$  looking at  $E(1)_{OUT}$ :

$$I(3 \rightarrow 1) = 1/4(1/3 - \sqrt{3}/3)[1 - \cos\varphi_{Tb} - \sin\varphi_{Tb}] = 0 \quad (6.5)$$

The solution in this case is  $\varphi_{Tb} = 90^\circ$ . If, instead, we had  $\varphi_1 = -60^\circ$  and  $\varphi_{ref} = 60^\circ$  the solution would be  $\varphi_{Tb} = -90^\circ$ .

**Tritter A setting** Finally we can set the first tritter of the interferometer. The light has to be injected in input 1 or 2 while the output can be any of the three. Also in this step we have to detect the minimum light power to set the phase of tritter A at  $90^\circ$  or  $-90^\circ$ . It is important to notice that this last setting depends on the goodness of the first two, since the outputs are influenced by all the set parameters. The proof is pretty much the same of tritter B, always keeping the setting of the previous stage as initial conditions.

Once both tritters have been set to their correct working points, it is possible to obtain an analytical expression which sum up how the intensity at the device outputs varies with respect to the interferometric phases when light is injected in one of the three inputs. For instance considering input 1 and output  $n = 1, 2, 3$  we can write:

$$I_n = 1/9[3 + 2\cos(\varphi_1 - \varphi_2 + \theta_n) + 2\cos(\varphi_2 - \varphi_{ref} + \theta_n) + 2\cos(\varphi_{ref} - \varphi_1 + \theta_n)] \quad (6.6)$$

where the phase shift  $\theta_n$  is a constant value which depends on the specific output under consideration.

## 6.4 Experimental data

Following the three-steps algorithm just explained, we performed the characterization of the three-arm interferometer, with the aim of retrieving the values of the  $\alpha$  coefficients for every active phase shifter placed in the internal interferometer modes. Despite we designed the device for having six of such resistors, our final device actually presents only four working ones (namely

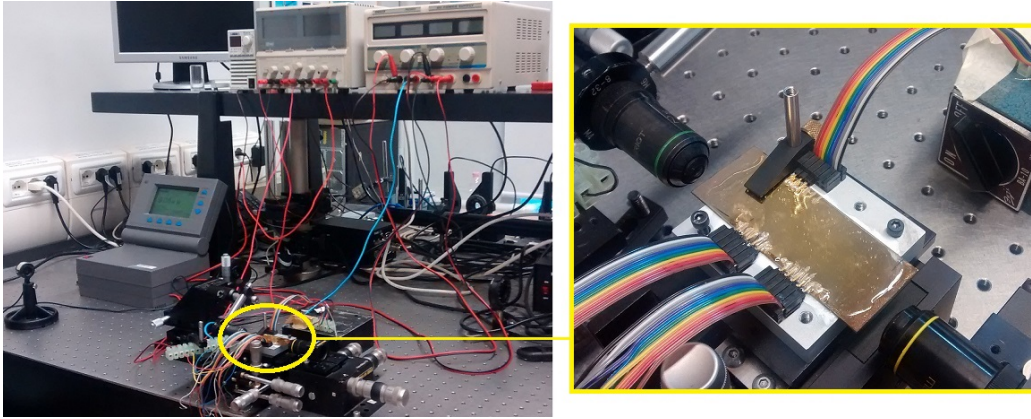


**Figure 6.7:** *On the left the setup for the characterization of the three-arm interferometer. On the right the device mounted between the two objectives.*

R1, R2, R3 and R4 in fig. 6.7), because the other two got irreversibly damaged during the connectorization stage.

The setup is shown in picture 6.7. The device is always put between the two objectives 10X (for light in-coupling) and 25X (for light out-coupling) and it is mounted on an aluminum base, in order to dissipate the heat generated by the electric power flowing in the resistor that avoids to reach too high temperatures. The collected light at the device output impinges on the head of a power meter. Besides the two tritters, two resistors on two different arms are connected to the power supply with a dynamic up to 10 V. We need to drive four resistors manually to reach the final setting.

### 6.4.1 Data acquisition

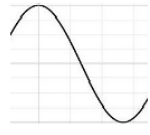
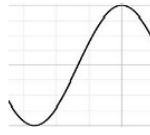
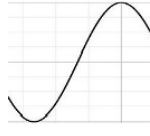
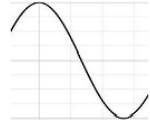
We decide to work with the resistors R1 and R2 (as named fig.6.1b) starting from the initial configuration obtained by the algorithm explained in the previous paragraph.

The configuration obtained is the one expected from theory, in agreement with fig. 6.8. This is the situation we get when, assuming the tritters set on  $90^\circ$ , the phase induced by R1 is  $+60^\circ$  respect to R2. Indeed if the phase were  $-60^\circ$  the output-spots would be shifted.

At this point we perform the following set of measurements: we couple light to

SET	OUTPUT1	OUTPUT2	OUTPUT3
INPUT1	1	0	0
INPUT2	0	0	1
INPUT3	0	1	0

**Figure 6.8:** Theoretical situation input/output once the setting, following the algorithm, is complete. This in the case the phase set with  $R1$  is  $+60^\circ$  respect to  $R2$ , assuming the tritters phase of  $90^\circ$ .

TRITTER A	OUTPUT1	OUTPUT2	OUTPUT3
INPUT1		0	
INPUT2		0	
INPUT3	0	1	0

**Figure 6.9:** Theoretical situation varying the voltage at the resistor of tritter A. Experimental data and theoretical prediction are in agreement looking at fig.6.10.

all input ports, and, for each one, we monitor the light intensity at each device output, when a scan in the voltage is applied to the different resistors. Before every scan, we restore the device settings to the its initial configuration. Taking these measurements we always pay attention to avoid a dissipation power too close to 1 W. In some trials we noticed, indeed, that at that power the resistors start to be damaged. We start by performing a power scan on tritter A for verifying its correct functioning. The experimental results obtained are plotted in fig.6.10 , and they can be compared to the theoretical predictions, shown in fig.6.9. It was already discussed how, obviously, the light injected from input 3 is not affected by the tuning of tritter A phase.



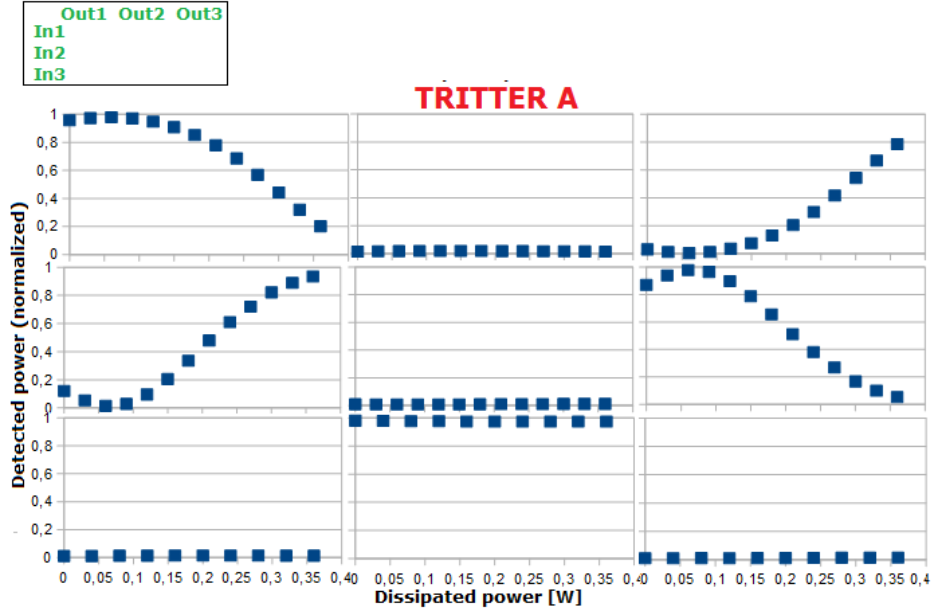


**Figure 6.10:** *Experimental data of tritter A. They are in agreement with the theoretical expectations (fig.6.9.)*

We have also two other constant outputs, entering from input 2. This is also in agreement with the theory since the analytical expression of this output is:

$$I(2 \rightarrow 1)_{TrB} = \left| \frac{e^{(i\varphi_{Tb})}}{2} + i \frac{e^{(i\varphi_{Tb})}}{2} + k^* \right|^2 = k \quad (6.7)$$

where  $k$  is a constant value.

The same measurement was performed also by scanning the voltage applied to tritter B and very similar results have been obtained.

We then proceeded by performing the voltage scan on R1 and R2, for the actual extrapolation of the  $\alpha$  coefficients. The curves acquired are shown in fig. 6.11, while the data analysis is discussed in the next paragraph.

### 6.4.2 Determination of the $\alpha$ coefficients

We want at this point to extrapolate the values of the  $\alpha$  coefficients from the curves of fig. 6.11. Re-calling eq.6.6 we can re-write it with a change of variables, instead of the phases we explicit the dependence of the output

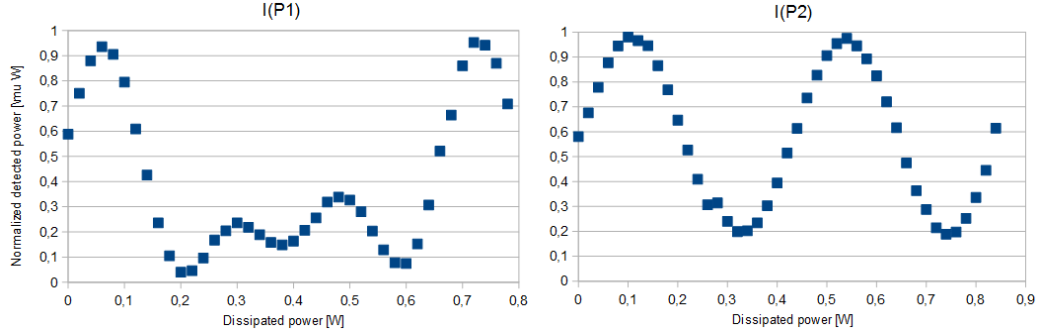


**Figure 6.11:** Curves acquired varying, respectively, the power dissipated from R1 and from R2. Both plots are for input 1 output 1, all the others I/O combinations are translated curves.

intensities from the dissipated powers (eq.6.3). What we get is:

$$I(P1) = \frac{1}{9}(3 + 2\cos(\alpha_{11}P1) + 2\cos(\alpha_{21}P1) + 2\cos((\alpha_{11} - \alpha_{21})P1)) \quad (6.8)$$

$$I(P2) = \frac{1}{9}(3 + 2\cos(\alpha_{22}P2) + 2\cos(\alpha_{12}P2) + 2\cos((\alpha_{12} - \alpha_{22})P2)) \quad (6.9)$$

where P1 and P2 are the dissipated power related to the voltage we impose on the resistor. Thus we have the overlap of three sinusoids whose frequencies are directly related to the coefficients we want to determine. In order to extrapolate these frequencies we perform numerically the Fourier transform of the curves acquired (fig.6.11).

The results we get are shown in fig.6.12. In the first plot we have the three-frequencies varying P1, in particular the first peak is the difference of the other two. The second plot resolves just one frequency. This is because, for the resistor R2, the value of the cross talk is really low, also by simulation, and so it is not distinguishable by the continuum component.

We would have to acquire more data and periods but it was not possible since the limited dynamics we can reach. This limitation is not given only by the apparatus but also because going beyond 0.9 W start to damage the resistors.

We also acquired and calculate the Fourier transform for the last two available resistors, R3 and R4. Their curve is of the same kind of R1. The values

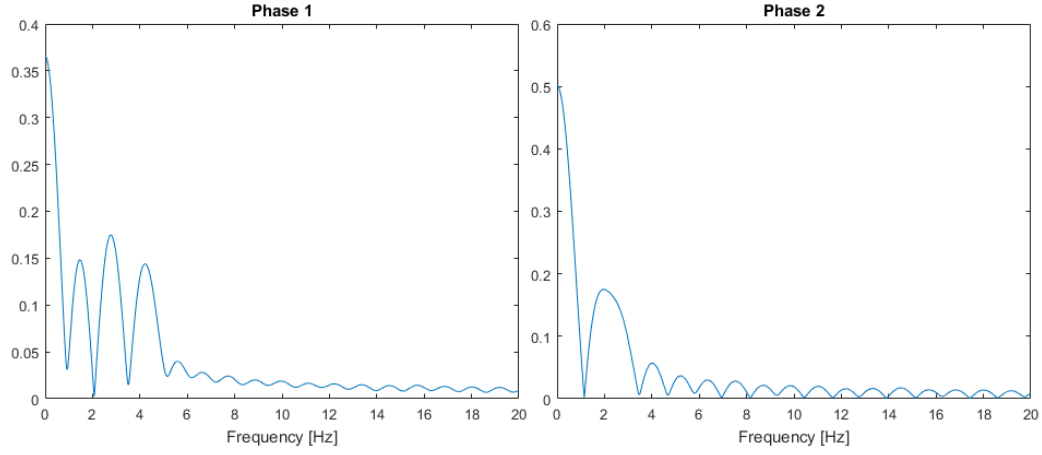


**Figure 6.12:** *Fourier Transform for the two curves of fig.6.11.*

of the so obtained  $\alpha$  coefficients (which correspond to the frequencies extrapolated by the Fourier analysis and multiplied by a factor  $2\pi$ ) are here reported:

$$\begin{pmatrix} \varphi_1 \\ \varphi_2 \end{pmatrix} = \begin{pmatrix} 25.76 & 0 \\ 17.03 & 13.01 \end{pmatrix} \begin{pmatrix} P_1 \\ P_2 \end{pmatrix} \quad (6.10)$$

$$\begin{pmatrix} \varphi_3 \\ \varphi_2 \end{pmatrix} = \begin{pmatrix} 25.95 & 0 \\ 17.40 & 13.01 \end{pmatrix} \begin{pmatrix} P_3 \\ P_2 \end{pmatrix} \quad (6.11)$$

$$\begin{pmatrix} \varphi_4 \\ \varphi_2 \end{pmatrix} = \begin{pmatrix} 28.84 & 0 \\ 19.35 & 13.01 \end{pmatrix} \begin{pmatrix} P_4 \\ P_2 \end{pmatrix} \quad (6.12)$$

From these results we notice the symmetry between phases  $\varphi_1$ ,  $\varphi_3$  and  $\varphi_4$ , as expected since they are in a symmetric position respect the central arm, especially  $\varphi_1$  and  $\varphi_3$ . We remember, once again, that these phases are phases difference since they are always refer to a reference  $\varphi_{ref}$ .

### 6.4.3 Interferometer's map

A peculiar plot regarding the trend of the phase difference is the one in fig.6.13 where the normalized measured power at the output is shown as a function of both phases.

In the first image, which refers to the first output entering from input 1,

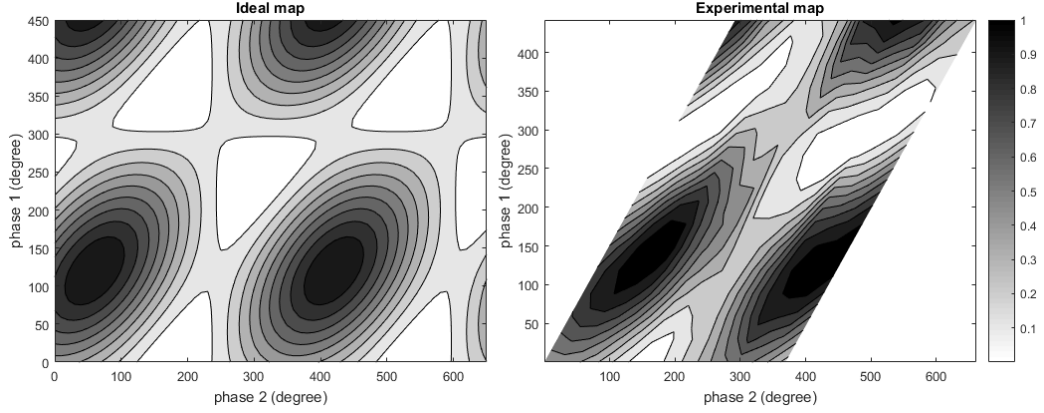


**Figure 6.13:** *The curve levels show the power detected at the output (in this case the first output from input 1) respect to the phase difference between  $\varphi_1$  and  $\varphi_2$ . On the left the map of an ideal interferometer, on the right the one obtained with ours. The section of this second is due to the crosstalk between the phase control.*

is shown the theoretical plot for an ideal interferometer. We find that the points of minimum are in positions where the phase difference is  $60^\circ$  or  $180^\circ$ . In the second image are reported the data acquired varying the powers which tune the two phases. The plot is stretched because of the crosstalk of the power P1 on the phase  $\varphi_2$ . Thus every time we change P1, it gives an offset to phase  $\varphi_2$ . Instead the crosstalk between power P2 and  $\varphi_1$  is not so evident, as we expected by the  $\alpha$  coefficients (eq.6.12). Comparing the two plots we notice a similar pattern. The main difference is that the areas of the minimum in the experimental plot are linked. A possible explanation of this behavior is an error in the values of the reflectivities and transmittivities of the couplers of the tritters. In particular, as it is possible to see from fig.6.14, by simulation we can have a more similar situation putting splitting ratios slightly higher than the ideals. If, instead, the splitting coefficients were lower than the ideals we would have the link in the other direction. The experimental points of minimum are, correctly, at a phase difference of  $60^\circ$  or  $180^\circ$ .

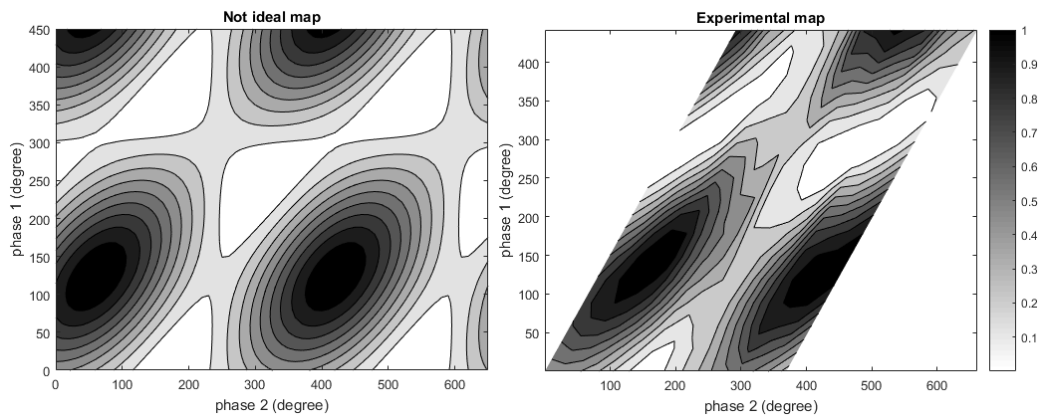


**Figure 6.14:** Comparison between a simulated not ideal map and the experimental one we get. The splitting coefficients in the simulation are of 0.54 (ideal 0.50) and 0.34 (ideal 1/3).

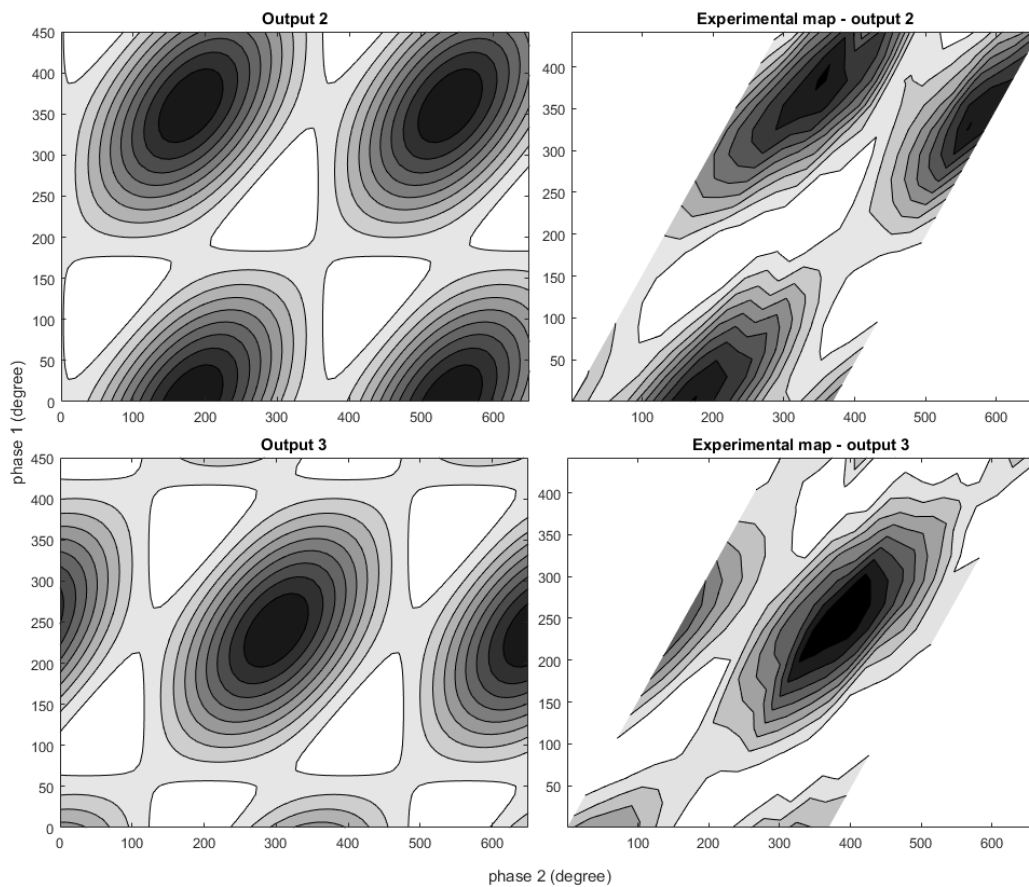


**Figure 6.15:** Comparison between the simulated ideal maps and the experimental ones For outputs 2 and 3.



# Conclusions

In this thesis work we have presented the design, the fabrication and the characterization with classical light of an integrated photonic device, which works as a three-modes interferometer. Thanks to the integration of several active phase shifters, it is possible to actively tune in a accurate way all the device internal phases, and this is testified by the observation of interference fringes at the circuit output, with almost unitary visibility and in a very good agreement with theoretical predictions. Such a device finds very important applications in the field of quantum metrology, and, in particular, for the implementation of super-resolved multi-parameters estimation algorithms. Experiments in this direction will be performed in the near future at Università La Sapienza, in Rome, employing the device described in this work. Remarkably, both the optical and the electrical components of the presented photonic device have been entirely fabricated by means of FLM, confirming that this microfabrication technique offers a unique degree of versatility and reliability for the development of integrated optical circuits with complex functionalities.

In future several kinds of experiments could be implemented thanks to the high possibility of tuning different phases which let to reach a great flexibility in the use of the device.





# Bibliography

- [1] BIPM. <http://www.bipm.org>.
- [2] V.B. Braginski and Y. I. Vorontsov. Quantum-mechanical limitations in macroscopic experiments and modern experimental technique. *Soviet Physics Uspekhi*, 17(5):644, 1975.
- [3] M. T. Jaekel and S. Reynaud. Quantum limits in interferometric measurements. *Europhysics Letters*, 13(4):301, 1990.
- [4] S. Lloyd V. Giovannetti and L. Maccone. Quantum-enhanced measurements: beating the standard quantum limit. *Science*, 306(5700):1330–1336, 2004.
- [5] H.P. Robertson. The uncertainty principle. *Physical Review*, 34(1):163, 1929.
- [6] L. Mandelstam and I. Tamm. The uncertainty relation between energy and time in nonrelativistic quantum mechanics. *J. Phys.(USSR)*, 9(249):1, 1945.
- [7] Z.Y. Ou. Fundamental quantum limit in precision phase measurement. *Physical Review A*, 55(4):2598, 1997.
- [8] D.J. Wineland J.J. Bollinger, W.M. Itano and D.J.Heinzen. Optimal frequency measurements with maximally correlated states. *Physical Review A*, 54(6):R4649, 1996.
- [9] C.M. Caves. Quantum-mechanical noise in an interferometer. *Physical Review D*, 23(8):1693, 1981.

- [10] J. L. O'Brien K. Sasaki T. Nagata, R. Okamoto and S. Takeuchi. Beating the standard quantum limit with four-entangled photons. *Science*, 316(5825):726–729, 2007.
- [11] S. Lloyd V. Giovannetti and L. Maccone. Quantum metrology. *Physical review letters*, 96(1):010401, 2006.
- [12] T. Nagata J.L. O'Brien K. Sasaki R. Okamoto, H. F. Hofmann and S. Takeuchi. Beating the standard quantum limit: phase super-sensitivity of n-photon interferometers. *New Journal of Physics*, 10(7):073033, 2008.
- [13] R. Prevedel A. Gilchrist G. J. Pryde J. L. O'Brien K. J. Resch, K. L. Pagnell and A. G. White. Time-reversal and super-resolving phase measurements. *Physical review letters*, 98(22):223601, 2007.
- [14] M.A. Taylor and W.P. Bowen. Quantum metrology and its application in biology. *Physics Reports*, 615:1–59, 2016.
- [15] S. Pang and T.A. Brun. Quantum metrology for a general hamiltonian parameter. *Physical Review A*, 90(2):022117, 2014.
- [16] O. Ambar I. Afek and Y. Silberberg. High-noon states by mixing quantum and classical light. *Science*, 328(5980):879–881, 2010.
- [17] C. Gerry P. and Knight. *Introductory quantum optics*. Cambridge university press, 2005.
- [18] L. Zehnder. *Ein neuer interferenzrefraktor*. Springer, 1891.
- [19] S.F. Adams K.P. Zetie and R.M. Tocknell. How does a mach-zehnder interferometer work? *Physics Education*, 35(1):46, 2000.
- [20] G. Roger P. Grangier and A. Aspect. Experimental evidence for a photon anticorrelation effect on a beam splitter: a new light on single-photon interferences. *Europhysics Letters*, 1(4):173, 1986.

- [21] Z. Ou C.K. Hong and L. Mandel. Measurement of subpicosecond time intervals between two photons by interference. *Physical Review Letters*, 59(18):2044, 1987.
- [22] J.P. Dowling. Quantum optical metrology—the lowdown on high-n00n states. *Contemporary physics*, 49(2):125–143, 2008.
- [23] C. Vitelli A. Crespi R. Ramponi R. Osellame P. Mataloni N. Spagnolo, L. Aparo and F. Sciarrino. Quantum interferometry with three-dimensional geometry. *Scientific reports*, 2:862, 2012.
- [24] J.C.F. Matthews A. Politi C.R. Neal R. Ramponi R. Osellame A. Crespi, M. Lobino and J.L. O’Brien. Measuring protein concentration with entangled photons. *Applied Physics Letters*, 100(23):233704, 2012.
- [25] T. Pellizzari A.K. Ekert M.B. Plenio S.F. Huelga, C. Macchiavello and J Ignacio J.I. Cirac. Improvement of frequency standards with quantum entanglement. *Physical Review Letters*, 79(20):3865, 1997.
- [26] N.F. Ramsey. A molecular beam resonance method with separated oscillating fields. *Physical Review*, 78(6):695, 1950.
- [27] S. Lloyd V. Giovannetti and L. Maccone. Quantum-enhanced positioning and clock synchronization. *Nature*, 412(6845):417–419, 2001.
- [28] P.G. Kwiat A.M. Steinberg and R.Y. Chiao. Dispersion cancellation in a measurement of the single-photon propagation velocity in glass. *Physical review letters*, 68(16):2421, 1992.
- [29] J. Borregaard and Anders S A.S. Sørensen. Near-heisenberg-limited atomic clocks in the presence of decoherence. *Physical review letters*, 111(9):090801, 2013.
- [30] LIGO Scientific Collaboration et al. A gravitational wave observatory operating beyond the quantum shot-noise limit. *Nature Physics*, 7(12):962–965, 2011.

- [31] N. Sugimoto K.M. Davis, K. Miura and K. Hiraoi. Writing waveguides in glass with a femtosecond laser. *Optics letters*, 21(21):1729–1731, 1996.
- [32] G. Cerullo R. Osellame and R. Ramponi. *Femtosecond laser micro-machining: photonic and microfluidic devices in transparent materials*, volume 123. Springer Science & Business Media, 2012.
- [33] K. Miura S. Kanehira and K. Hirao. Ion exchange in glass using femtosecond laser irradiation. *Applied Physics Letters*, 93(2):023112, 2008.
- [34] G.D. Marshall D.J. Little P. Dekker, M. Ams and M.J. Withford. Annealing dynamics of waveguide bragg gratings: evidence of femtosecond laser induced colour centres. *Optics express*, 18(4):3274–3283, 2010.
- [35] R. Brückner. Properties and structure of vitreous silica. i. *Journal of non-crystalline solids*, 5(2):123–175, 1970.
- [36] S. Risbud J.W. Chan, T. Huser and D.M. Krol. Structural changes in fused silica after exposure to focused femtosecond laser pulses. *Optics letters*, 26(21):1726–1728, 2001.
- [37] Y. Shimotsuma K. Miura M. Sakakura, M. Shimizu and K. Hirao. Temperature distribution and modification mechanism inside glass with heat accumulation during 250 khz irradiation of femtosecond laser pulses. *Applied Physics Letters*, 93(23):231112, 2008.
- [38] L. Huang R.J. Finlay T-H Her J. Paul Callan E.N. Glezer, M. Milosavljevic and E. Mazur. Three-dimensional optical storage inside transparent materials. *Optics Letters*, 21(24):2023–2025, 1996.
- [39] S.M. Eaton. *Contrasts in thermal diffusion and heat accumulation effects in the fabrication of waveguides in glasses using variable repetition rate femtosecond laser*. PhD thesis, University of Toronto, 2008.
- [40] M.L. Ng J. Li-W. Chen S. Ho S. M. Eaton, H. Zhang and Peter R P.R. Herman. Transition from thermal diffusion to heat accumulation in high repetition rate femtosecond laser writing of buried optical waveguides. *Optics express*, 16(13):9443–9458, 2008.

- [41] G. Vallone P. Mataloni A. Crespi R. Ramponi L. Sansoni, F. Sciarrino and R. Osellame. Polarization entangled state measurement on a chip. *Physical review letters*, 105(20):200503, 2010.
- [42] N. Chiodo D. Polli R.M. Vazquez R. Ramponi R. Osellame, V. Maselli and G. Cerullo. Fabrication of 3d photonic devices at 1.55/ $\mu\text{m}$  wavelength by femtosecond ti: Sapphire oscillator. *Electronics Letters*, 41(6):315–317, 2005.
- [43] A. Yariv. Coupled-mode theory for guided-wave optics. *IEEE Journal of Quantum Electronics*, 9(9):919–933, 1973.
- [44] A.M. Streltsov and N.F. Borrelli. Fabrication and analysis of a directional coupler written in glass by nanojoule femtosecond laser pulses. *Optics Letters*, 26(1):42–43, 2001.
- [45] H. Zhang R. Iyer J. Li M.L Ng S. Ho J.S. Aitchison S.M. Eaton, W-J Chen and Peter R P.R. Herman. Spectral loss characterization of femtosecond laser written waveguides in glass with application to demultiplexing of 1300 and 1550 nm wavelengths. *Journal of Lightwave Technology*, 27(9):1079–1085, 2009.
- [46] Ch Santschi E. Grenet R. Eckert O.J.F. Martin M. Guillaumée, L.A. Dunbar and R.P. Stanley. Polarization sensitive silicon photodiodes using nanostructured metallic grids. *Applied Physics Letters*, 94(19):193503, 2009.
- [47] M.A. Horne Z. Marek, A. Zeilinger et al. Realizable higher-dimensional two-particle entanglements via multiport beam splitters. *Physical Review A*, 55(4):2564, 1997.
- [48] H.J. Bernstein M. Reck, A. Zeilinger and P. Bertani. Experimental realization of any discrete unitary operator. *Physical Review Letters*, 73(1):58, 1994.

- [49] M. Huber S. Ramelow C. Schaeff, R. Polster and A. Zeilinger. Experimental access to higher-dimensional entangled quantum systems using integrated optics. *Optica*, 2(6):523–529, 2015.
- [50] E.P. Ippen J.G. Fujimoto A.M. Kowalevich, V. Sharma and K. Minoshima. Three-dimensional photonic devices fabricated in glass by use of a femtosecond laser oscillator. *Optics letters*, 30(9):1060–1062, 2005.
- [51] S. Gross G.D. Marshall M.J. Steel T. Meany, M. Delanty and M.J. Withford. Non-classical interference in integrated 3d multiports. *Optics express*, 20(24):26895–26905, 2012.
- [52] L. Aparo P. Mataloni F. Sciarrino A. Crespi R. Ramponi N. Spagnolo, C. Vitelli and R. Osellame. Three-photon bosonic coalescence in an integrated tritter. *Nature communications*, 4:1606, 2013.
- [53] E.P. Ippen K. Minoshima, A.M. Kowalevich and James G J.G. Fujimoto. Fabrication of coupled mode photonic devices in glass by nonlinear femtosecond laser materials processing. *Optics Express*, 10(15):645–652, 2002.
- [54] C. Florea and K.A. Winick. Fabrication and characterization of photonic devices directly written in glass using femtosecond laser pulses. *Journal of Lightwave Technology*, 21(1):246, 2003.
- [55] L.G. Helt M.J. Withford Z. Chaboyer, T. Meany and M.J. Steel. Tunable quantum interference in a 3d integrated circuit. *Scientific reports*, 5:9601, 2015.
- [56] R. Ramponi D. J. Brod E. F. Galvão N. Spagnolo C. Vitelli E. Maiorino P. Mataloni A. Crespi, R. Osellame and F. Sciarrino. Integrated multimode interferometers with arbitrary designs for photonic boson sampling. *Nature Photonics*, 7(7):545–549, 2013.
- [57] A.S. Rab N. Spagnolo V. D’ambrosio P. Mataloni F. Sciarrino T. Zan-drini A. Crespi R. Rampon F. Flamini, L. Magrini et al. Thermally-

- reconfigurable quantum photonic circuits at telecom wavelength by femtosecond laser micromachining. *arXiv preprint arXiv:1512.04330*, 2015.
- [58] G. Corrielli. *Integrated photonic circuits by femtosecond laser writing for qubit manipulation, quantum cryptography and quantum-optical analogies*. PhD thesis, Politecnico di Milano, 2015.
- [59] J. Dörring U. Morgner M.J. Lederer D. Kopf A. Killi, A. Steinmann and C. Fallnich. High-peak-power pulses from a cavity-dumped yb: Ky (wo 4) 2 oscillator. *Optics letters*, 30(14):1891–1893, 2005.
- [60] A. Killi and U. Morgner. Solitary pulse shaping dynamics in cavity-dumped laser oscillators. *Optics express*, 12(15):3397–3407, 2004.
- [61] M. Gräfe S. Nolte R. Heilmann, R. Keil and A. Szameit. Ultraprecise phase manipulation in integrated photonic quantum circuits with generalized directional couplers. *Applied Physics Letters*, 105(6):061111, 2014.